



OPEN Thermosolutal convection in a baffled curvilinear porous cabinet filled with magneto radiative hybrid nanofluid

Samrat Hansda^{1✉}, Anirban Chattopadhyay², Swapan K. Pandit³ & Hakan F. Öztop^{4,5,6}

This study focuses on optimizing the thermosolutal performance of a wavy porous cabinet with a T-shaped cold baffle, highlighting the utilization of a radiative Cu-Al₂O₃-water hybrid nanoliquid and diverse heating strategies. The purpose of this work is to evaluate the influence of these factors on hydromagnetic thermosolutal behavior under the influence of various thermal boundary conditions. By employing an efficient Higher Order Compact (HOC) scheme, the Navier-Stokes equations in streamfunction (ψ)-vorticity (ζ) form and energy as well as species transport equations are solved. In a novel approach, the study introduces a T-shaped cold baffle in the middle of the container, introducing complexity to the porous configuration. The investigation encompasses three distinct heating scenarios: uniform heating and soluting of the lower border (Case-1), linear heating and soluting (Case-2), and non-uniform heating and soluting (Case-3), while maintaining the side walls at cold and low concentration. The upper wall remains adiabatic. The results reveal a significant improvement in energy transfer across all cases, with an increase of 467.12% for Case-1, 470.98% for Case-2, and 387.78% for Case-3 as the radiation parameter (Rd) is varied from 1 to 10. In contrast, solutal transfer experiences a slight decline, quantified as 3.09% for Case-1, 2.05% for Case-2, and 6.07% for Case-3. These findings emphasize the superior thermosolutal performance of Case-1, where an optimized heating strategy significantly enhances the overall system efficiency. This study provides valuable insights for improving thermal management systems in practical applications. Notably, in areas such as electronic device cooling, heat exchangers, and porous industrial processes, the findings offer the potential for enhanced efficiency and reliability.

Keywords T-shaped baffle, Different heating strategy, Energy and solutes transfer, Hybrid nanofluid, Higher order compact scheme (HOC), Thermal radiation, Irreversibility

Abbreviations

Pr	Prandtl number
Ra	Rayleigh number
Da	Darcy number
Ha	Hartmann number
B_0	Magnetic effect ($\text{Amp } m^{-1}$)
Rd	Radiation parameter
D	Mass diffusivity, ($m^2 s^{-1}$)
g	Gravitational acceleration (ms^{-2})
Le	Lewis number, $Le = \frac{\alpha}{D}$
N	Buoyancy ratio parameter, $N = \frac{Gr_C}{Gr_T}$
k	Thermal conductivity ($Wm^{-1}K^{-1}$)
p	Dimensional pressure (Nm^{-2})

¹Department of Mathematics, Sidho-Kanho-Birsha University, 723104 Purulia, West Bengal, India. ²Department of Mathematics, Government General Degree College, 722135 Ranibandh, Bankura, West Bengal, India. ³Integrated Science Education & Research Centre (ISERC), Visva-Bharati, 731235 Santiniketan, West Bengal, India. ⁴Department of Mechanical Engineering, Technology Faculty, Firat University, 23119 Elazig, Turkey. ⁵Department of Medical Research, China Medical University Hospital, Taichung, Taiwan. ⁶University Centre for Research & Development, Chandigarh University, 140413 Mohali, Punjab, India. ✉email: samrat-hansda@skbu.ac.in

P	Dimensionless pressure
T	Dimensional temperature
C	Dimensional concentration
c	Dimensionless concentration
C_p	Specific heat ($\text{J Kg}^{-1}\text{K}^{-1}$)
\overline{Nu}	Average Nusselt number
\overline{Sh}	Average Sherwood number
x, y	Dimensional Cartesian coordinates (m)
X, Y	Dimensionless Cartesian coordinates
u, v	Dimensional velocities in x, y directions respectively (ms^{-1})
U, V	Dimensionless velocities in X, Y directions respectively
ξ, η	Dimensionless coordinate in computational plane
E_{HT}	Total entropy generation due to heat transfer
E_{FF}	Total entropy generation due to fluid friction
E_{MT}	Total entropy generation due to mass transfer
E_{MF}	Total entropy generation due to magnetic field
E_T	Total entropy generation
Be	Bejan number
m	Shape factor of hybrid nanoparticles

Greek letters

α	Thermal diffusivity (m^2s^{-1})
β	Thermal expansion coefficient (K^{-1})
ϕ	Volume fraction of the hybrid nanoparticles
ρ	Hybrid nanofluid density (Kg m^{-3})
ν	Kinematic viscosity (m^2s^{-1})
μ	Dynamic viscosity (Pa s)
ψ	Stream function
ζ	Vorticity
σ	Electrical conductivity ($\mu \text{ S cm}^{-1}$)
θ	Dimensionless temperature

Subscripts

i, j	Cell faces
f	Fluid
nf	Nanofluid
hmf	Hybrid nanofluid
hnp	Hybrid nanoparticles

Double-diffusive or thermosolutal convection (TC), arising from the simultaneous influence of thermal and solutal gradients has garnered considerable attention in fluid dynamics and energy transport. This phenomenon, commonly referred to as thermosolutal or double-diffusive convection (DDC), plays a pivotal role in various disciplines, including oceanography, astrophysics, biology, geology, engineering, and chemical processes¹⁻⁵.

Recent advancements in nanofluid dynamics have provided deeper insights into the intricate interplay of thermal transport and magnetohydrodynamic (MHD) effects in complex systems. Baithalu et al.⁶ investigated CNT nanofluid flow over rotating discs using the Darcy-Forchheimer model, while Panda et al.⁷ explored slip velocity effects in radiative hybrid nanofluids. Furthermore, Baithalu et al.⁸ examined magnetic dissipation in radiative free convection, whereas Panda et al.⁹ analyzed the impact of inertial drag on chemically reactive polar nanofluids, elucidating the role of MHD forces in heat and mass transfer. Additionally, Mishra et al.¹⁰ leveraged machine learning techniques to predict transient CNT nanomaterial flow, demonstrating the potential of artificial intelligence in thermal analysis. Pattnaik et al.¹¹ conducted an EMHD sensitivity analysis on hybrid nanofluids, emphasizing the influence of variable magnetization and heat generation on transport phenomena. In this context, one may find notable contributions in¹²⁻²¹, which further enrich the theoretical and computational framework of nanotechnology. These studies collectively underscore the critical role of hybrid nanofluids, radiative heat transfer, and computational modeling in advancing thermal management strategies and optimizing energy-efficient systems.

In recent decades, numerous studies on TC have been undertaken by researchers. For instance, Kumar et al.²² conducted a numerical study using the Lattice Boltzmann Method to examine species and thermal transport. Corcione et al.²³ explored thermosolutal free convection induced by opposing horizontal species and energy gradients in a square cavity. Rashid et al.²⁴ comprehensively investigated solutal and energy transfer in Magnetohydrodynamics (MHD) Casson fluid flow within a crown chamber, revealing the dual effect of manipulating the Casson parameter on thermal performance and species transfer. Highlighting the pivotal role played by Magnetohydrodynamics (MHD) convection, Aly et al.²⁵ carried out a numerical investigation on TC within a baffled cavity loaded with nanoliquid. Their study revealed a diminishing thermosolutal performance as the Hartmann number (Ha) increased. By using Darcy-Brinkman-Forchheimer Model, Moderres et al.²⁶ examined TC in a horizontal annulus filled with a porous medium. In their work, they have analyzed the behavior of flow topology, energy, and solutal transfer for various parameters. Aly et al.²⁷ investigated the effect of a rotating circular cylinder with paddles on TC inside a square nanofluid chamber. They noticed that as ϕ increases to 6%, $|\psi|_{max}$ is diminished by 10.76% whereas $|\psi|_{min}$ is reduced by 75.54% as Ha increases to 100.

Using the incompressible smoothed particle hydrodynamics (ISPH) method, Aly and Mohamed²⁸ analyzed DDC in a cavity loaded with copper-water nanofluid. They showed that the buoyancy ratio (N) changes the directions of the solid particle's diffusion within the system. In addition, Elshehaby et al.²⁹ carried TC in an L-shaped enclosure with baffles by using the ISPH method and artificial intelligence. In a related exploration, Chamkha and Al-Naser³⁰ delved into the realm of MHD TC inside a rectangular container. Their study highlighted a notable reduction in fluid circulation and energy transfer attributable to the presence of a magnetic field. In a study on double diffusion with a magnetic field, Teamah³¹ concluded that species and energy transfer remained unchanged for $Ha > 20$. Hansda and Pandit³² explored a comprehensive simulation on double diffusion inside a partially heated wavy container, revealing a noteworthy impact of Ha on reducing thermosolutal transfer rates. Notably, there is a gap in studies considering the impact of wavy walls on the optimum heat transfer of hybrid nanofluids in closed cavities. The existing research highlights a scarcity of studies on the double diffusive behavior of hybrid nanofluids aimed at finding the optimum heat transfer.

In an alternative domain, thermal radiation, an often overlooked yet the essential method of heat transfer in such contexts plays a leading role as a means of energy transportation through waves. As an illustration, Srinivasacharya and Ramana³³ revealed heightened energy transfer within an inclined wavy nanoliquid enclosure with an augmented radiation parameter. Ibrahim and Lemonnier³⁴ investigated the dynamics of time-dependent DDC flow with radiation in a square chamber, highlighting the observation that radiation accelerated thermal performance within the chamber. In a related vein, Moufekkir et al.³⁵ utilized simulations to explore the interplay of TC and volumetric radiation through the multiple relaxation time lattice Boltzmann (MRT-LBM) method, revealing modifications in thermosolutal distribution and flow topology induced by volumetric radiation. Examining the effects of radiative energy transfer on TC, Abidi et al.³⁶ carried out investigations using a cubic cabinet subjected to differential heating. Similarly, Mohammadi and Nassab³⁷ explored the influences of Soret-Dufour effects and radiation on TC. In the domain of TC, Rashad et al.³⁸ studied an investigation delving into the intricate interplay between chemical reactions and the thermal radiation phenomenon. Simultaneously, there has been a noteworthy increase in the examination of baffles' role inside various cavities, becoming a significant area of interest across scientific and engineering disciplines^{39,40}. A noteworthy study by Chamkha et al.⁴¹ delves into TC within an inclined triangular porous cabinet featuring a fin. Their findings demonstrate that skillful manipulation of the heat absorption/generation parameter effectively enhances thermosolutal transfer within the system. Similarly, in a study conducted by Al-Farhany et al.⁴², MHD TC inside a curvilinear container loaded with $Fe_3O_4-H_2O$ ferrofluid was explored. The incorporation of two baffles on inclined borders resulted in augmentations in thermosolutal transfer with increasing baffle presence. Additionally, Eshaghi et al.⁴³ investigated DDC in a finned H-shaped cavity, revealing optimal energy transfer conditions for a fin at $+60^\circ$ and higher solutal transfer for a fin at -60° . DDC in a C-shaped container equipped with wavy fines has been examined by Nayak et al.⁴⁴. They observed enhancements in streamlines as the amplitude of the wavy baffle increased. Investigating the impact of oscillating fines on DDC in nanoparticle-enhanced phase change materials (NEPCM) suspensions inside an asteroid-shaped chamber, Alsedais and Aly⁴⁵ found that expanded inner baffles yielded higher values of \overline{Nu} and \overline{Sh} .

In parallel, Irshad et al.⁴⁶ scrutinized double diffusion in an H-shaped porous wavy container with two baffles, contributing additional dimensions to our understanding of the interplay between convective processes and baffles. Collectively, these research endeavor significantly to enrich the evolving field of convective mass and heat transfer. However, a notable gap remains in exploring the effects of wavy walls, diverse baffle types, and the application of both hybrid and double diffusive nanofluids, representing potential avenues for future investigations.

In scheming any thermodynamics system, the entropy generation (EG) plays a vital role which manifests the thermal energy losses in every system⁴⁷. In 1982, Bejan discovered the concept of entropy generation (EG) which includes all types of heat and mass transport processes⁴⁸. In this context, Zahor et al.⁴⁹ conducted a review to study the roles of various parameters on entropy generation. In this context, using a single-phase nanofluid model, Sheremet et al.⁵⁰ investigated EG and heat transfer inside a wavy container. They observed that the nanoparticle volume fraction (ϕ) could increase the Bejan number. Utilizing, compact finite-difference lattice Boltzmann method (CFDLBM), KhakRah et al.⁵¹ surveyed the nanofluid flow and energy transfer performance of a wavy cavity. They noticed that Nu_{avg} augments with enlarging Ra and ϕ . In their study, they also found that

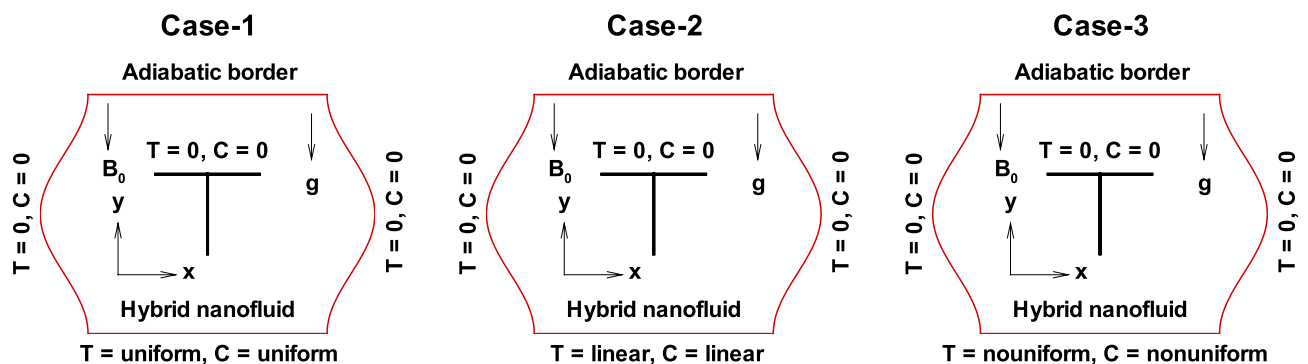


Fig. 1. Physical configurations for the problem.

Physical properties	H ₂ O	Cu (s ₁)	Al ₂ O ₃ (s ₂)
ρ (Kg m ⁻³)	997.1	8933	3970
C_p (J Kg ⁻¹ K ⁻¹)	4179	385	765
k (W m ⁻¹ K ⁻¹)	0.613	400	40
β (K ⁻¹)	21×10^{-5}	5.01×10^{-5}	2.55×10^{-5}
σ (μ S/cm)	0.05	5.97×10^7	1.0×10^{-10}
μ (Kg m ⁻¹ s ⁻¹)	8.55×10^{-4}	—	—
Pr	5.83	—	—

Table 1. Thermophysical properties of H₂O, Cu, Al₂O₃⁷⁸.

Properties	Nanofluids model
Density	$\rho_{hnf} = (1 - \phi_2) \left\{ (1 - \phi_1)\rho_f + \phi_1\rho_{s1} \right\} + \phi_2\rho_{s2}$
Viscosity	$\frac{\mu_{hnf}}{\mu_f} = (1 - \phi_1)^{-2.5} (1 - \phi_2)^{-2.5}$
Specific heat capacity	$(\rho c_p)_{hnf} = (1 - \phi_2) \left\{ (1 - \phi_1)(\rho c_p)_f + \phi_1(\rho c_p)_{s1} \right\} + \phi_2(\rho c_p)_{s2}$
Thermal expansion coefficient	$(\rho\beta)_{hnf} = (1 - \phi_2) \left\{ (1 - \phi_1)(\rho\beta)_f + \phi_1(\rho\beta)_{s1} \right\} + \phi_2(\rho\beta)_{s2}$
Thermal conductivity	$\frac{k_{hnf}}{k_f} = \frac{k_{s2} + (m - 1)k_{nf} + (m - 1)\phi_2(k_{s2} - k_{nf})}{k_{s2} + (m - 1)k_{nf} - \phi_2(k_{s2} - k_{nf})}$, where, $\frac{k_{nf}}{k_f} = \frac{k_{s1} + (m - 1)k_f + (m - 1)\phi_1(k_{s1} - k_f)}{k_{s1} + (m - 1)k_f - \phi_1(k_{s1} - k_f)}$
Thermal diffusivity	$\alpha_{hnf} = \frac{k_{hnf}}{(\rho C_p)_{hnf}}$
Electrical conductivity	$\frac{\sigma_{hnf}}{\sigma_{nf}} = \frac{\sigma_{s2} + 2\sigma_{nf} + 2\phi_2(\sigma_{s2} - \sigma_{nf})}{\sigma_{s2} + 2\sigma_{nf} - \phi_2(\sigma_{s2} - \sigma_{nf})}$, where, $\frac{\sigma_{nf}}{\sigma_f} = \frac{\sigma_{s1} + 2\sigma_f + 2\phi_1(\sigma_{s1} - \sigma_f)}{\sigma_{s1} + 2\sigma_f - \phi_1(\sigma_{s1} - \sigma_f)}$
Solutal diffusivity	$D_{hnf} = (1 - \phi_1)(1 - \phi_2)D_f$

Table 2. Physical attributes of Cu-Al₂O₃/H₂O hybrid nanoliquid^{32,79–82}.

ϕ could increase EG. Inside trapezoidal chamber, Shirvan et al.⁵² analyzed a sensitivity analysis of free convection and EG of Al₂ O₃-water nanofluid. Their results showed that Nu_{avg} and EG improve with Ra . Tayebi et al.⁵³ scrutinized the impact of magnetic field and conducting wavy solid block on EG and natural convection within a hybrid nanofluid loaded enclosure. They indicated that the conductivity ratio of the wavy solid block and the magnetic field could significantly affect EG within the system. Ishak et al.⁵⁴ explored the roles of finite wall thickness on EG and heat transfer inside Al₂ O₃-water nanoliquid filled square container. They revealed that the thickness of the solid wall could control the Bejan number and heat transfer within the enclosure. Magherbi et al.⁵⁵ carried out EG for TC and found that the values of EG escalated with the thermal Grashof number at

Different shapes of nanoparticle	Numerical values (m)
Spherical	3
Bricks	3.7
Cylindrical	4.8
Platelet	5.7
Blades	8.6

Table 3. Shape factor for different nanoparticles⁸¹.

lower Lewis numbers. Using Darcy-Brinkman formulation, Mchirgui et al.⁵⁶ simulated EG for TC in a porous enclosure. Oueslati et al.⁵⁷ have examined TC with EG within a partially active container. EG and TC in a solar dryer were investigated by Ghachem et al.⁵⁸ and observed lower values of EG at $N = 1$. Ababaei et al.⁵⁹ have investigated EG of thermosolutal mixed convection in a right-angled trapezoidal cavity and noticed that the overall generated entropy increases dramatically when the heater moves toward the cold boundary. Hussain et al.⁶⁰ carried out the thermosolutal forced and free convection in a cavity filled with nanoliquid. They noticed the effect of EG and controlling parameters on the species and energy transport efficiency.

The review of available literature spotlights the growing interest in thermosolutal convection with hybrid nanofluids, emphasizing its increasing importance. While there have been investigations into the thermosolutal performance of hybrid nanofluids within enclosed domains, addressing the increasing demand for efficient thermal systems, a comprehensive exploration of the energy transport phenomenon is essential. To impart a specific heating effect to a particular thermal system, a thorough examination of the enhancements in heat and mass transfer understanding is imperative. A notable gap persists in understanding and optimizing the complex dynamics of mass and heat transfer within complex cavities under the influence of various thermal boundary conditions. This prompts the recurring question: What category of heating strategy constitutes the optimal choice for a specific thermal system? Addressing this inquiry necessitates a vital step—an exhaustive comparative evaluation that considers uniform, linear, and nonuniform heating approaches. The combination of growing demand and a shortage of existing research propels our enthusiasm to explore the present work. Based on the literature review, the identified research gaps, the objectives of this study, and its novelties are outlined below:

Research gaps identified based on literature review

Despite significant advancements in the study of thermosolutal convection, several critical research gaps remain unaddressed. A comprehensive exploration of energy transport phenomena in thermosolutal convection involving hybrid nanofluids within complex geometries is still lacking. The intricate dynamics of heat and mass transfer within complex cavities, particularly under varying thermal boundary conditions in the presence of a T-shaped baffle has not been thoroughly investigated. Additionally, there is an absence of comparative evaluations of different heating strategies—such as uniform, linear, and nonuniform heating—to determine the most efficient approach for specific thermal applications. Moreover, limited research exists on double-diffusive natural convection (DDNC) involving hybrid Cu-Al₂O₃/water nanoliquids in wavy (convex) enclosures, particularly in the presence of a T-shaped baffle. This gap underscores the need for further exploration into how geometric modifications and nanofluid compositions influence thermosolutal performance. Addressing these research gaps is crucial for optimizing thermal management systems in engineering applications.

To bridge these gaps, the present study investigates the thermosolutal behavior of radiative hybrid nanofluids within a convex enclosure embedded in porous media. Particular attention is given to the role of a T-shaped cold fin and its impact on energy and mass transport. By analyzing these factors, this research aims to provide deeper insights into the optimization of heat transfer in complex enclosures.

Objectives of the study

This study aims to analyze comprehensively the interplay between a T-shaped baffle, a wavy enclosure, and radiative hybrid nanofluids to understand their collective influence on thermosolutal performance. A key focus is on entropy generation, which serves as a metric for assessing the efficiency of heat and mass transfer processes. Furthermore, the study conducts a comparative evaluation of different heating strategies namely uniform, linear, and nonuniform to identify the optimal thermal management approach. By leveraging detailed simulations and theoretical analysis, the research seeks to recommend the best configuration for superior energy efficiency across various engineering applications.

Novel contributions of the study

This research presents several novel contributions to the field of thermal sciences. It provides a pioneering investigation into the combined effects of a T-shaped baffle, a wavy (convex) cavity, and radiative hybrid nanofluids on double-diffusive natural convection. By integrating entropy generation analysis, the study offers valuable insights into optimizing heat and mass transfer mechanisms within complex geometries under different heating strategies. Additionally, the role of the T-shaped baffle in modifying nanofluid dynamics within a complex enclosure is explored in depth, revealing its potential to enhance thermal performance. By bridging existing research gaps, this study contributes to a more comprehensive understanding of hybrid nanofluids in intricate enclosures, offering valuable implications for real-world applications such as drying processes, solar collectors, electronics cooling, advanced heat exchangers, and renewable energy systems.

Problem formulations and mathematical modelings

Problem configuration

The visual representation of the problem configuration in this investigation is shown in Fig. 1. In this setup, a porous container with a wavy structure (of convex nature) is completely saturated with radiative copper (Cu) and aluminum oxide (Al₂O₃) nanoparticles. The lower boundary of the container is subjected to heating and solute injection, while the side walls are kept at cold and low concentration. The upper boundary of the enclosure is treated as adiabatic. All four boundaries of the enclosure remain stationary. Additionally, a T-shaped cold fin is located in the middle of the chamber. An external magnetic field is enforced parallel to gravity. The thermophysical attributes of the primary fluid, copper (Cu) nanoparticles, and aluminum oxide (Al₂O₃) nanoparticles are extensively outlined in Table 1. Additionally, Table 2 offers a detailed compilation of the inherent properties of the hybrid nanofluid composed of Cu, Al₂O₃, and water. The configuration-specific shape factors (m) for distinct nanoparticles are provided in Table 3.

Fundamental equations

This investigation is centered on the exploration of a laminar, steady, Newtonian, viscous, and incompressible flow inside a 2D container. The fluid under investigation is a hybrid nanofluid consisting of Cu-Al₂O₃. Introducing the steady thermosolutal natural convection in this system, the governing equations can be succinctly expressed as follows^{81,83}:

$$\frac{\partial u}{\partial x} + \frac{\partial v}{\partial y} = 0, \quad (1)$$

$$u \frac{\partial u}{\partial x} + v \frac{\partial u}{\partial y} = -\frac{1}{\rho_{hnf}} \frac{\partial p}{\partial x} + \frac{\mu_{hnf}}{\rho_{hnf}} \left[\left(\frac{\partial^2 u}{\partial x^2} + \frac{\partial^2 u}{\partial y^2} \right) - \frac{u}{k^*} \right] - \frac{\sigma_{hnf}}{\rho_{hnf}} B_0^2 u, \quad (2)$$

$$u \frac{\partial v}{\partial x} + v \frac{\partial v}{\partial y} = -\frac{1}{\rho_{hnf}} \frac{\partial p}{\partial y} + \frac{\mu_{hnf}}{\rho_{hnf}} \left[\left(\frac{\partial^2 v}{\partial x^2} + \frac{\partial^2 v}{\partial y^2} \right) - \frac{v}{k^*} \right] + \frac{g}{\rho_{hnf}} \left[(\rho\beta_\theta)_{hnf} (\theta - \theta_c) - (\rho\beta_c)_{hnf} (c - c_c) \right], \quad (3)$$

$$u \frac{\partial \theta}{\partial x} + v \frac{\partial \theta}{\partial y} = \alpha_{hnf} \left[\frac{\partial^2 \theta}{\partial x^2} + \frac{\partial^2 \theta}{\partial y^2} \right] - \frac{1}{(\rho C_p)_{hnf}} \left[\frac{\partial r_{rx}}{\partial x} + \frac{\partial r_{ry}}{\partial y} \right], \quad (4)$$

$$u \frac{\partial c}{\partial x} + v \frac{\partial c}{\partial y} = D_{hnf} \left[\frac{\partial^2 c}{\partial x^2} + \frac{\partial^2 c}{\partial y^2} \right]. \quad (5)$$

In equation (4), the term $-\frac{1}{(\rho C_p)_{hnf}} \left[\frac{\partial r_{rx}}{\partial x} + \frac{\partial r_{ry}}{\partial y} \right]$ is responsible for radiation effect. r_{rx} and r_{ry} can be written by employing Rosseland approximation^{81,83} as follows:

$$r_{rx} = -\frac{16\sigma^* \theta_c^3}{3\beta_\theta} \frac{\partial \theta}{\partial x}, \quad r_{ry} = -\frac{16\sigma^* \theta_c^3}{3\beta_\theta} \frac{\partial \theta}{\partial y}. \quad (6)$$

The system of equations (1)-(5) are transformed into non-dimensional form and are written as follows

$$\frac{\partial U}{\partial X} + \frac{\partial V}{\partial Y} = 0, \quad (7)$$

Wall	Imposed conditions
Baffle	$U = 0 = V, \psi = 0, T=0, C=0$
Top border	$U = 0, V = 0, \psi = 0, \frac{\partial T}{\partial Y} = 0, \frac{\partial C}{\partial Y} = 0$
Side borders	$U = 0 = V, \psi = 0, T = 0, C=0$
Bottom border	$U = 0 = V, \psi = 0$
	$T = 1, C = 1$ (Case-1)
	$T = 1 - X, C = 1 - X$ (Case-2)
	$T = \sin \pi X, C = \sin \pi X$ (Case-3)

Table 4. The non-dimensional boundary conditions for the considered problem.

$$U \frac{\partial U}{\partial X} + V \frac{\partial U}{\partial Y} = -\frac{\partial P}{\partial X} + \frac{\mu_{hnf}}{\rho_{hnf} \alpha_f} \left[\left(\frac{\partial^2 U}{\partial X^2} + \frac{\partial^2 U}{\partial Y^2} \right) - \frac{U}{Da} \right] - \frac{\sigma_{hnf}}{\sigma_f} \frac{\rho_f}{\rho_{hnf}} Ha^2 Pr U, \quad (8)$$

$$U \frac{\partial V}{\partial X} + V \frac{\partial V}{\partial Y} = -\frac{\partial P}{\partial Y} + \frac{\mu_{hnf}}{\rho_{hnf} \alpha_f} \left[\left(\frac{\partial^2 V}{\partial X^2} + \frac{\partial^2 V}{\partial Y^2} \right) - \frac{V}{Da} \right] + \frac{(\rho\beta\theta)_{hnf}}{\rho_{hnf} \beta_f} Ra Pr (T + NC), \quad (9)$$

$$U \frac{\partial T}{\partial X} + V \frac{\partial T}{\partial Y} = \frac{\alpha_{hnf}}{\alpha_f} \left(1 + \frac{4}{3} Rd \frac{k_f}{k_{hnf}} \right) \left[\frac{\partial^2 T}{\partial X^2} + \frac{\partial^2 T}{\partial Y^2} \right], \quad (10)$$

$$U \frac{\partial C}{\partial X} + V \frac{\partial C}{\partial Y} = \frac{D_{hnf}}{D_f} \frac{1}{Le} \left(\frac{\partial^2 C}{\partial X^2} + \frac{\partial^2 C}{\partial Y^2} \right), \quad (11)$$

where, $P = \frac{\rho L^2}{\rho_{hnf} \alpha_f^2}$, $X = \frac{x}{L}$, $Y = \frac{y}{L}$, $U = \frac{uL}{\alpha_f}$, $V = \frac{vL}{\alpha_f}$, $T = \frac{\theta - \theta_c}{\theta_h - \theta_c}$, $C = \frac{c - c_c}{c_h - c_c}$, $Le = \frac{\alpha_f}{D_f}$, $Ha = B_0 L \sqrt{\frac{\sigma_f}{\rho_f \nu_f}}$, $Da = \frac{k^*}{L^2}$, $Pr = \frac{\nu_f}{\alpha_f}$, $Rd = \frac{4\sigma^* \theta_c^3}{k_f \beta_\theta}$, $Ra = \frac{g \beta_f (\theta_h - \theta_c) L^3}{\alpha_f \nu_f}$ and $N = \frac{(\beta c)_{hnf} (c_h - c_c)}{(\beta\theta)_{hnf} (\theta_h - \theta_c)}$.

In order to remove the pressure term, we have employed the streamfunction (ψ) and vorticity (ζ) formulation and equations (7)-(11) are written as follows

$$-\frac{\partial^2 \psi}{\partial X^2} - \frac{\partial^2 \psi}{\partial Y^2} = \zeta, \quad (12)$$

$$-\frac{\mu_{hnf}}{\rho_{hnf} \alpha_f} \left(\frac{\partial^2 \zeta}{\partial X^2} + \frac{\partial^2 \zeta}{\partial Y^2} \right) + U \frac{\partial \zeta}{\partial X} + V \frac{\partial \zeta}{\partial Y} + \frac{\mu_{hnf}}{\rho_{hnf} \alpha_f} \frac{1}{Da} \zeta = \frac{(\rho\beta\theta)_{hnf}}{\rho_{hnf} \beta_f} Ra Pr \left(\frac{\partial T}{\partial X} + N \frac{\partial C}{\partial X} \right) - \frac{\sigma_{hnf}}{\sigma_f} \frac{\rho_f}{\rho_{hnf}} \frac{\partial U}{\partial Y}, \quad (13)$$

$$-\frac{\alpha_{hnf}}{\alpha_f} \left(1 + \frac{4}{3} Rd \frac{k_f}{k_{hnf}} \right) \left[\frac{\partial^2 T}{\partial X^2} + \frac{\partial^2 T}{\partial Y^2} \right] + U \frac{\partial T}{\partial X} + V \frac{\partial T}{\partial Y} = 0, \quad (14)$$

$$-\frac{D_{hnf}}{D_f} \frac{1}{Le} \left(\frac{\partial^2 C}{\partial X^2} + \frac{\partial^2 C}{\partial Y^2} \right) + U \frac{\partial C}{\partial X} + V \frac{\partial C}{\partial Y} = 0, \quad (15)$$

where,

$$U = \frac{\partial \psi}{\partial Y}, \quad V = -\frac{\partial \psi}{\partial X}, \quad \zeta = \frac{\partial V}{\partial X} - \frac{\partial U}{\partial Y}. \quad (16)$$

Boundary conditions

The dimensionless boundary conditions for this study are displayed in Table 4

Thermal and species transfer activity

In this investigation, The average Nusselt (\overline{Nu}) and Sherwood number (\overline{Sh}) are evaluated by the following relations^{81,83}:

$$\overline{Nu} = \frac{k_{hnf}}{k_f} \left(1 + \frac{4}{3} Rd \frac{k_f}{k_{hnf}} \right) \int_0^1 \left(-\frac{\partial T}{\partial Y} \right) dX. \quad (17)$$

$$\overline{Sh} = \frac{D_{hnf}}{D_f} \int_0^1 \left(-\frac{\partial C}{\partial Y} \right) dX. \quad (18)$$

Analysis of entropy production

A thorough examination of entropy generation is included in the discussion of the problem. The dimensional representation of the entropy generation number is formulated in accordance with prior research findings^{2,61}:

$$\begin{aligned}
E_{gen} = & \frac{k_{hnf}}{\theta_0^2} \left[\left(\frac{\partial \theta}{\partial x} \right)^2 + \left(\frac{\partial \theta}{\partial y} \right)^2 \right] + \frac{\mu_{hnf}}{\theta_0} \left[2 \left(\frac{\partial u}{\partial x} \right)^2 + 2 \left(\frac{\partial v}{\partial y} \right)^2 + \left(\frac{\partial u}{\partial y} + \frac{\partial v}{\partial x} \right)^2 \right] \\
& + \frac{\mu_{hnf}}{k^* \theta_0} \left[u^2 + v^2 \right] + \frac{\sigma_{hnf}}{\theta_0} B_0^2 u^2 + \frac{RD_{hnf}}{c_0} \left[\left(\frac{\partial c}{\partial x} \right)^2 + \left(\frac{\partial c}{\partial y} \right)^2 \right] \\
& + \frac{RD_{hnf}}{\theta_0} \left[\left(\frac{\partial \theta}{\partial x} \right) \left(\frac{\partial c}{\partial x} \right) + \left(\frac{\partial \theta}{\partial y} \right) \left(\frac{\partial c}{\partial y} \right) \right]. \quad (19)
\end{aligned}$$

By employing $\left(\frac{k_f \Delta \theta^2}{\theta_0^2 L^2} \right)$ as typical scales, the dimensionless form of local entropy generation numbers are written as follows:

- Heat transfer

$$E_{lht} = \frac{k_{hnf}}{k_f} \left[\left(\frac{\partial T}{\partial X} \right)^2 + \left(\frac{\partial T}{\partial Y} \right)^2 \right],$$

- Fluid friction

$$E_{lff} = \varphi_1 \frac{\mu_{hnf}}{\mu_f} \left[2 \left(\frac{\partial U}{\partial X} \right)^2 + 2 \left(\frac{\partial V}{\partial Y} \right)^2 + \left(\frac{\partial U}{\partial Y} + \frac{\partial V}{\partial X} \right)^2 + \frac{1}{Da} \left(U^2 + V^2 \right) \right],$$

- Magnetic field:

$$E_{lmf} = \varphi_1 \frac{\sigma_{hnf}}{\sigma_f} Ha^2 U^2$$

- Mass transfer

$$E_{lmt} = \frac{D_{hnf}}{D_f} \left\{ \varphi_2 \left[\left(\frac{\partial C}{\partial X} \right)^2 + \left(\frac{\partial C}{\partial Y} \right)^2 \right] + \varphi_3 \left[\left(\frac{\partial T}{\partial X} \right) \left(\frac{\partial C}{\partial X} \right) + \left(\frac{\partial T}{\partial Y} \right) \left(\frac{\partial C}{\partial Y} \right) \right] \right\}, \quad (20)$$

where, $\varphi_1 = \frac{\mu_f \theta_0}{k_f} \left[\frac{\alpha_f}{L(\theta_h - \theta_c)} \right]^2$, $\varphi_2 = \frac{RD_f}{k_f c_0} \left(\theta_0 \frac{c_h - c_l}{\theta_h - \theta_c} \right)^2$ and $\varphi_3 = \frac{RD_f}{k_f} \left(\theta_0 \frac{c_h - c_l}{\theta_h - \theta_c} \right)$. For this simulation, $\varphi_1 = 10^{-4}$, $\varphi_2 = 0.5$ and $\varphi_3 = 10^{-2}$ ^(2,61). In addition, the total entropy generation (E_T) is evaluated by

$$E_T = E_{HT} + E_{FF} + E_{MF} + E_{MT}, \quad (21)$$

where, $E_{HT} = \int_{\Omega} E_{lht} d\Omega$, $E_{FF} = \int_{\Omega} E_{lff} d\Omega$, $E_{MF} = \int_{\Omega} E_{lmf} d\Omega$, and $E_{MT} = \int_{\Omega} E_{lmt} d\Omega$. Also, the Bejan number (Be) is defined as follows

$$Be = \frac{E_{HT} + E_{MT}}{E_T}. \quad (22)$$

The physical significance of the Bejan number (Be) is limited by its numerical values, $Be > 0.5$ implies dominance of heat transfer irreversibility and $Be < 0.5$ indicates dominance of fluid friction irreversibility.

Discretization and numerical procedure

The non-dimensional equations (12)-(15) can be written under the same umbrella of the 2D general second degree equation

$$\begin{aligned}
a(x, y) \frac{\partial^2 \Phi}{\partial x^2} + b(x, y) \frac{\partial^2 \Phi}{\partial y^2} + c(x, y) \frac{\partial \Phi}{\partial x} + d(x, y) \frac{\partial \Phi}{\partial y} \\
+ p(x, y) \Phi = \chi \left(x, y, \frac{\partial \theta_1}{\partial x}, \frac{\partial \theta_1}{\partial y}, \frac{\partial \theta_2}{\partial x}, \frac{\partial \theta_2}{\partial y} \right), \quad (23)
\end{aligned}$$

where, $a(x, y)$, $b(x, y)$ are the diffusion coefficients, $c(x, y)$ and $d(x, y)$ are the convection coefficients, $p(x, y)$ is the coefficient in the reaction term and r.h.s of (23) is the source term containing derivatives. Now, we have adopted the transformation technique and discretization procedure as given in Pandit and Chattopadhyay⁶². As such, we have considered the following co-ordinate transformation function

$$y = \xi,$$

$$x = 1 - \xi + A(2\xi - 1) + B \left[2\eta \cos(2\pi\eta) - \cos(2\pi\eta) \right].$$

The first and second order differential operators are given as follows:

$$\begin{bmatrix} \partial_x \\ \partial_y \end{bmatrix} = \frac{1}{|J|} \begin{bmatrix} y_\eta & -y_\xi \\ -x_\eta & x_\xi \end{bmatrix} \begin{bmatrix} \partial_\xi \\ \partial_\eta \end{bmatrix},$$

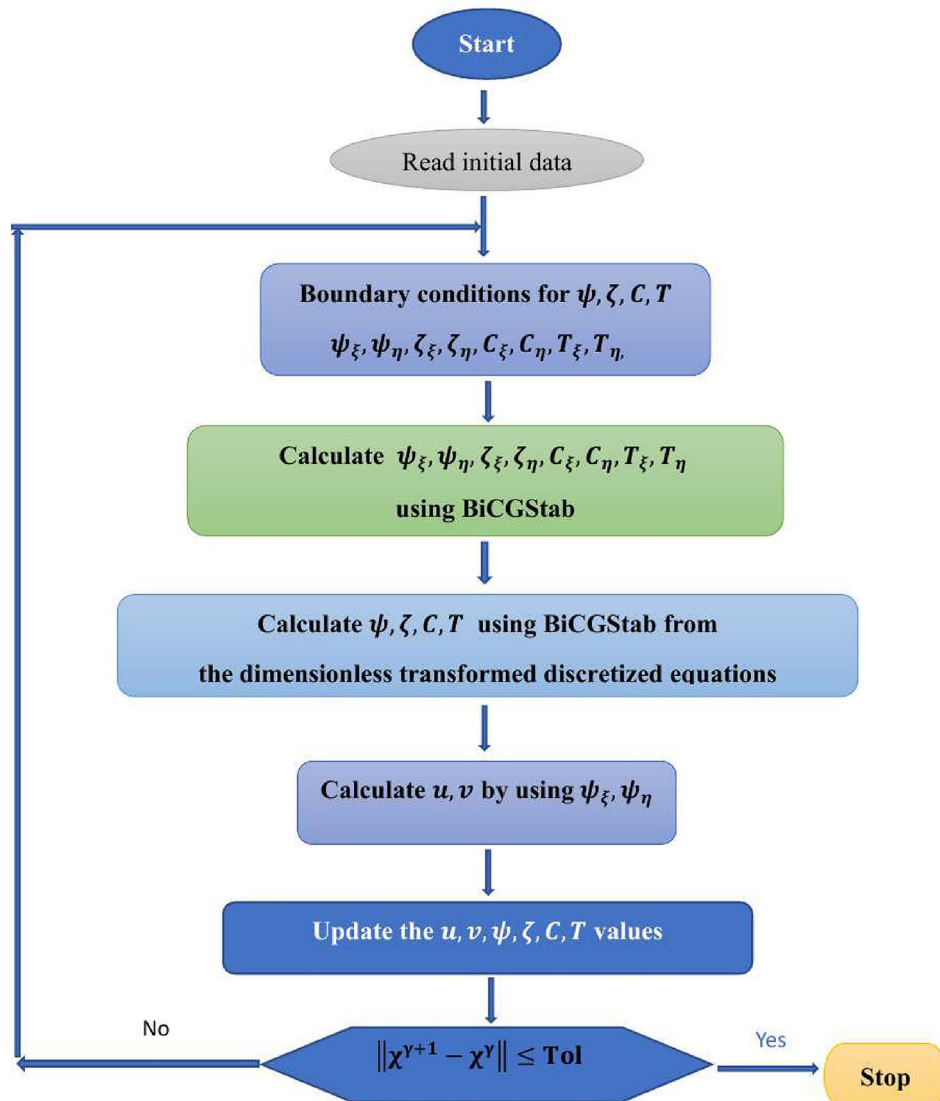


Fig. 2. Flow chart for solution algorithm.

$$\begin{aligned} \begin{bmatrix} \partial_{xx} \\ \partial_{yy} \end{bmatrix} &= \frac{1}{|J|^2} \left(\begin{bmatrix} y_\eta & -y_\xi & 0 & 0 \\ 0 & 0 & x_\xi & x_\eta \end{bmatrix} \begin{bmatrix} y_{\xi\eta} & -y_{\xi\xi} \\ y_{\eta\eta} & -y_{\eta\xi} \\ x_{\xi\eta} & x_{\xi\xi} \\ x_{\eta\eta} & -x_{\xi\xi} \end{bmatrix} \right) \begin{bmatrix} \partial_\xi \\ \partial_\eta \end{bmatrix} \\ &= \frac{1}{|J|^3} \left(\begin{bmatrix} y_\eta & -y_\xi & 0 & 0 \\ 0 & 0 & x_\xi & 0 \end{bmatrix} \begin{bmatrix} y_\eta & -y_\xi & 0 & 0 \\ 0 & y_\eta & -y_\xi & 0 \\ x_\xi & x_\xi & 0 & 0 \\ 0 & 0 & x_\eta & -x_\xi \end{bmatrix} \right) \begin{bmatrix} J_\xi & 0 \\ J_\eta & 0 \\ 0 & J_\xi \\ 0 & J_\eta \end{bmatrix} \begin{bmatrix} \partial_\xi \\ \partial_\eta \end{bmatrix} \\ &+ \frac{1}{|J|^2} \begin{bmatrix} y_\eta^2 & -2y_\xi y_\eta & y_\xi^2 \\ x_\eta^2 & -2x_\xi x_\eta & x_\xi^2 \end{bmatrix} \begin{bmatrix} \partial_{\xi\xi} \\ \partial_{\xi\eta} \\ \partial_{\eta\eta} \end{bmatrix} \end{aligned}$$

where J is the Jacobian matrix given by $J = \begin{bmatrix} x_\xi y_\eta - x_\eta y_\xi \end{bmatrix}$.

As in⁶², the fourth order accurate compact scheme for the equation (23) in the computational ξ - η plane is

$$\begin{aligned} &A'_{i,j} \delta_\xi^2 \hat{\phi}_{i,j} + G'_{i,j} \delta_\xi \delta_\eta \hat{\phi}_{i,j} + B'_{i,j} \delta_\eta^2 \hat{\phi}_{i,j} + C'_{i,j} \delta_\xi \hat{\phi}_{i,j} + D'_{i,j} \delta_\eta \hat{\phi}_{i,j} + H'_{i,j} \hat{\phi}_{i,j} \\ &+ \frac{1}{12} \left[X'_{i,j} \delta_\xi^2 \delta_\eta^2 \hat{\phi}_{i,j} + Y'_{i,j} \delta_\xi^2 \delta_\eta \hat{\phi}_{i,j} + Z'_{i,j} \delta_\xi \delta_\eta^2 \hat{\phi}_{i,j} \right] = F'_{i,j} \\ &+ \frac{g_{i,j}}{24} \left[\frac{1}{k} \left\{ 2(\hat{\phi}_\xi)_{i,j-1} - 2(\hat{\phi}_\xi)_{i,j+1} - (\hat{\phi}_\xi)_{i-1,j-1} - (\hat{\phi}_\xi)_{i+1,j-1} + (\hat{\phi}_\xi)_{i+1,j+1} + (\hat{\phi}_\xi)_{i-1,j+1} \right\} \right. \\ &+ \left. \frac{1}{h} \left\{ 2(\hat{\phi}_\eta)_{i-1,j} - 2(\hat{\phi}_\eta)_{i+1,j} - (\hat{\phi}_\eta)_{i-1,j-1} + (\hat{\phi}_\eta)_{i+1,j-1} + (\hat{\phi}_\eta)_{i+1,j+1} - (\hat{\phi}_\eta)_{i-1,j+1} \right\} \right] \\ &+ O(h^4, k^4), \end{aligned} \tag{24}$$

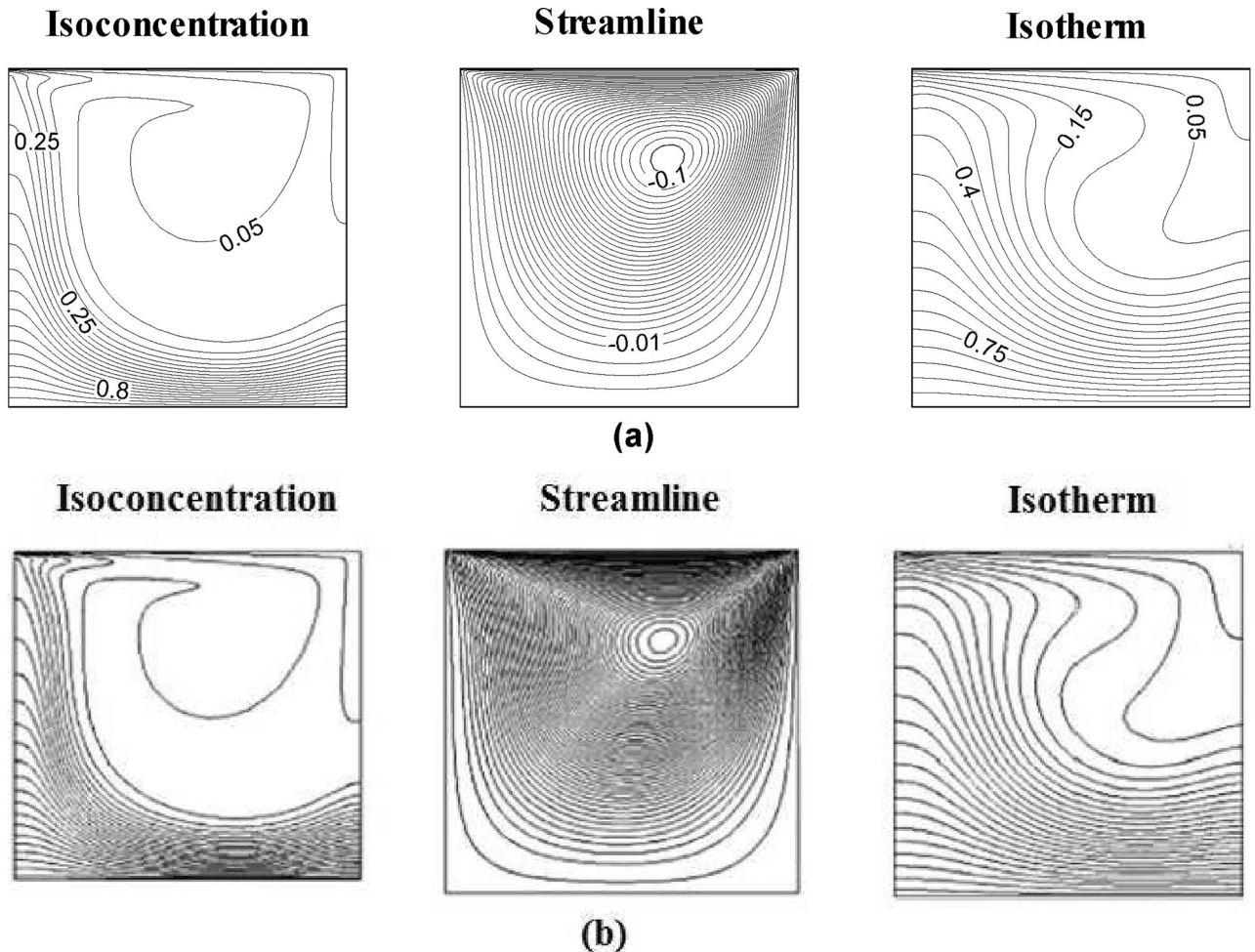


Fig. 3. Comparison of isoconcentrations, streamlines and isotherms contours (a) Present (b) Al-Amiri et al.⁶⁷.

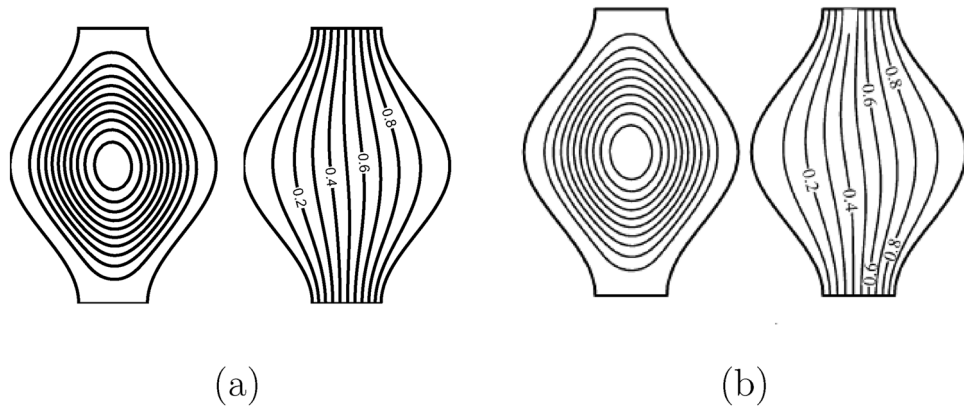


Fig. 4. Comparison of streamlines and isotherms contours (a) Present (b) Mahmud et al.⁶⁸.

where, h and k are the steps along ξ - and η - directions respectively and the coefficients $A', B', C', D', G', H', X', Y', Z'$ can be found in^{63–65}. In the same process, we can obtain F' for the present problem. The gradients $\hat{\phi}_\xi$ and $\hat{\phi}_\eta$, appeared in equations (24) are approximated compactly as tridiagonal system:

$$\hat{\phi}_{\xi i,j} = \left(\delta_\xi \hat{\phi}_{i,j} - \frac{h^2}{6} \delta_\xi^2 \hat{\phi}_{\xi i,j} \right) + O(h^4) \tag{25}$$

or

$$\frac{1}{6} \hat{\phi}_{\xi i+1,j} + \frac{4}{6} \hat{\phi}_{\xi i,j} + \frac{1}{6} \hat{\phi}_{\xi i-1,j} = \frac{\hat{\phi}_{i+1,j} - \hat{\phi}_{i-1,j}}{2h} \tag{26}$$

and

$$\hat{\phi}_{\eta i,j} = \left(\delta_\eta \hat{\phi}_{i,j} - \frac{k^2}{6} \delta_\eta^2 \hat{\phi}_{\eta i,j} \right) + O(k^4) \tag{27}$$

or

$$\frac{1}{6} \hat{\phi}_{\eta i,j+1} + \frac{4}{6} \hat{\phi}_{\eta i,j} + \frac{1}{6} \hat{\phi}_{\eta i,j-1} = \frac{\hat{\phi}_{i,j+1} - \hat{\phi}_{i,j-1}}{2k} \tag{28}$$

Interest readers may also look into the detailed formulations^{63–65}. The coefficient matrix resulting from the transformed equations is nonsymmetric and solved iteratively by the BiCGStab method⁶⁶. Our computed steady-state results are accumulated by fulfilling the following convergence criterion:

$$\max |\Omega_{i,j}^{(\gamma+1)} - \Omega_{i,j}^{(\gamma)}| < 0.5 \times 10^{-5}, \tag{29}$$

where, $\Omega_{i,j}^{(\gamma)}$ denotes numerical values at γ^{th} iteration representing the numerical values of $\psi_{i,j}, \zeta_{i,j}, T_{i,j}$ and $C_{i,j}$. To compute the steady solution of Navier-Stokes equations, we have employed an outer-inner iteration procedure with the following numerical algorithm

1. γ^{th} iteration: Initialize ψ, ζ, T, C, u, v .
2. $(\gamma + 1)^{\text{th}}$ iteration:
 - (a) Set the boundary condition for $\psi_\xi, \psi_\eta, \zeta_\xi, \zeta_\eta, T_\xi, T_\eta, C_\xi, C_\eta, u_\xi, u_\eta, v_\xi, v_\eta$.
 - (b) Compute $\psi_\xi, \psi_\eta, \zeta_\xi, \zeta_\eta, T_\xi, T_\eta, C_\xi, C_\eta, u_\xi, u_\eta, v_\xi, v_\eta$ at all points inside the domain by BiCGStab method.
3. (a) Solve for $T^{\gamma+1}$ using $u^\gamma, v^\gamma, T_\xi^{\gamma+1}, T_\eta^{\gamma+1}$. (b) Solve for $C^{\gamma+1}$ using $u^\gamma, v^\gamma, C_\xi^{\gamma+1}, C_\eta^{\gamma+1}$. (c) Solve for $\zeta^{\gamma+1}$ using $u^\gamma, v^\gamma, T_\xi^{\gamma+1}, T_\eta^{\gamma+1}, \zeta_\xi^{\gamma+1}, \zeta_\eta^{\gamma+1}, C_\xi^{\gamma+1}, C_\eta^{\gamma+1}$. (d) Solve for $\psi^{\gamma+1}$ using $\psi_\xi^{\gamma+1}, \psi_\eta^{\gamma+1}, \psi^{\gamma+1}$. (e) Compute $u^{\gamma+1}$ and $v^{\gamma+1}$ using $\psi_\xi^{\gamma+1}, \psi_\eta^{\gamma+1}$.

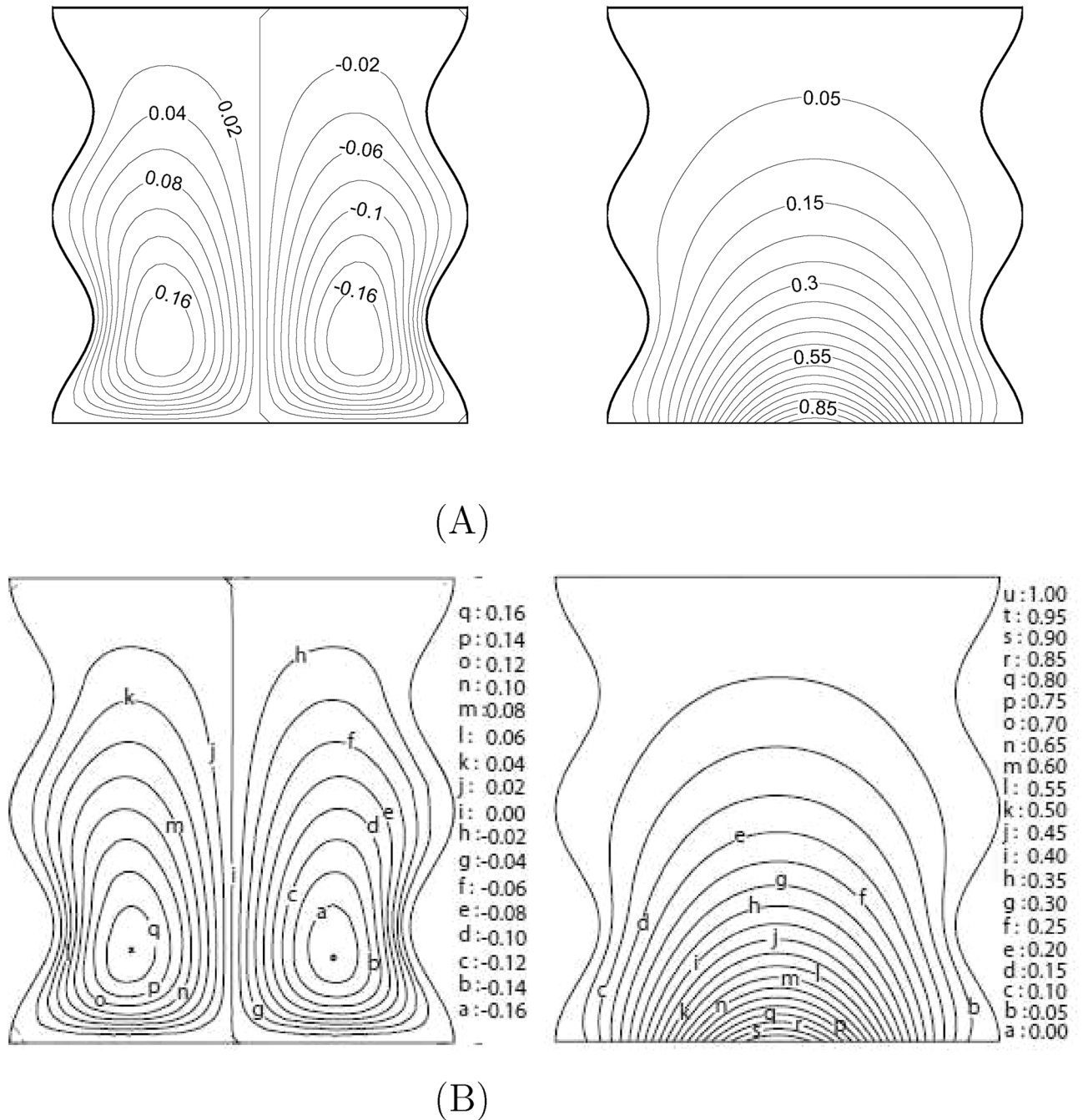


Fig. 5. Comparison of streamlines and isotherms contours (A) Present (B) Sompong et al.⁶⁹.

- Verify convergence of χ i.e. $\max |\chi_{i,j}^{(\gamma+1)} - \chi_{i,j}^{(\gamma)}| \leq \text{Tol}$ where, χ stands for ψ, ζ, T and C and Tol stands for tolerance limit.

This constitute one outer iteration cycle. Repeat steps 2, 3 until convergence. The flow chart of the solution algorithm is given in Fig. 2. It is mentioned here that all the computations in this study have been performed on an Intel quad-core processor-based PC with 8 GB RAM using C language. For this work, Tecplot software is used for graph presentation.

Validation of computational code and sensitivity analysis on grid resolution

In this subsection, the accuracy of our in-house computing code is assessed by reproducing the results of Al-Amiri et al.⁶⁷ in a square geometry constituting a single moving lid with uniform but different values of

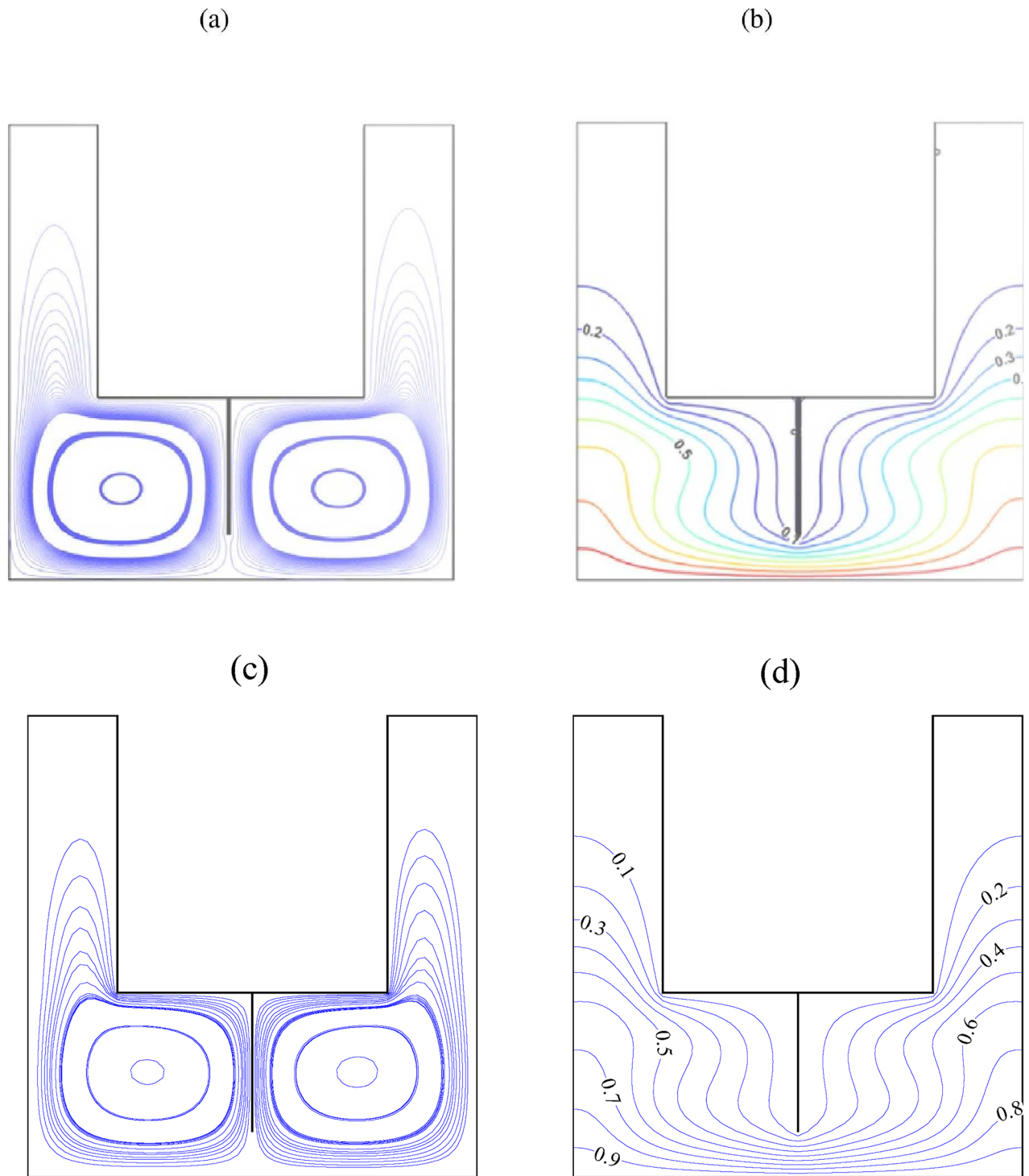


Fig. 6. Comparison of streamlines and isotherms between (i)⁷⁰ (a, b) and (ii) present work (c, d) for $Ra = 10^5$, $Ha = 20$, $AR = 0.6$, $\phi = 0.05$.

temperature and concentration for the bottom and top walls. As per their problem demonstration, the side walls are treated as impermeable, and in adiabatic conditions while the top lid is in motion toward the right. In Fig. 3, we have displayed the contours of streamline, temperature and concentration for $Pr = 1$, $Le = 10$, $Re = 10^2$ and $Ri = 10^{-2}$. It is seen that our results agreed well with those in Al-Amiri et al.⁶⁷. Qualitatively, we have also reproduced numerical results for streamlines and isotherms as shown in Fig. 4 for the case of free convection inside a wavy enclosure presented by Mahmud et al.⁶⁸. From the results, we have observed an excellent agreement between the results of Mahmud et al.⁶⁸ and our results.

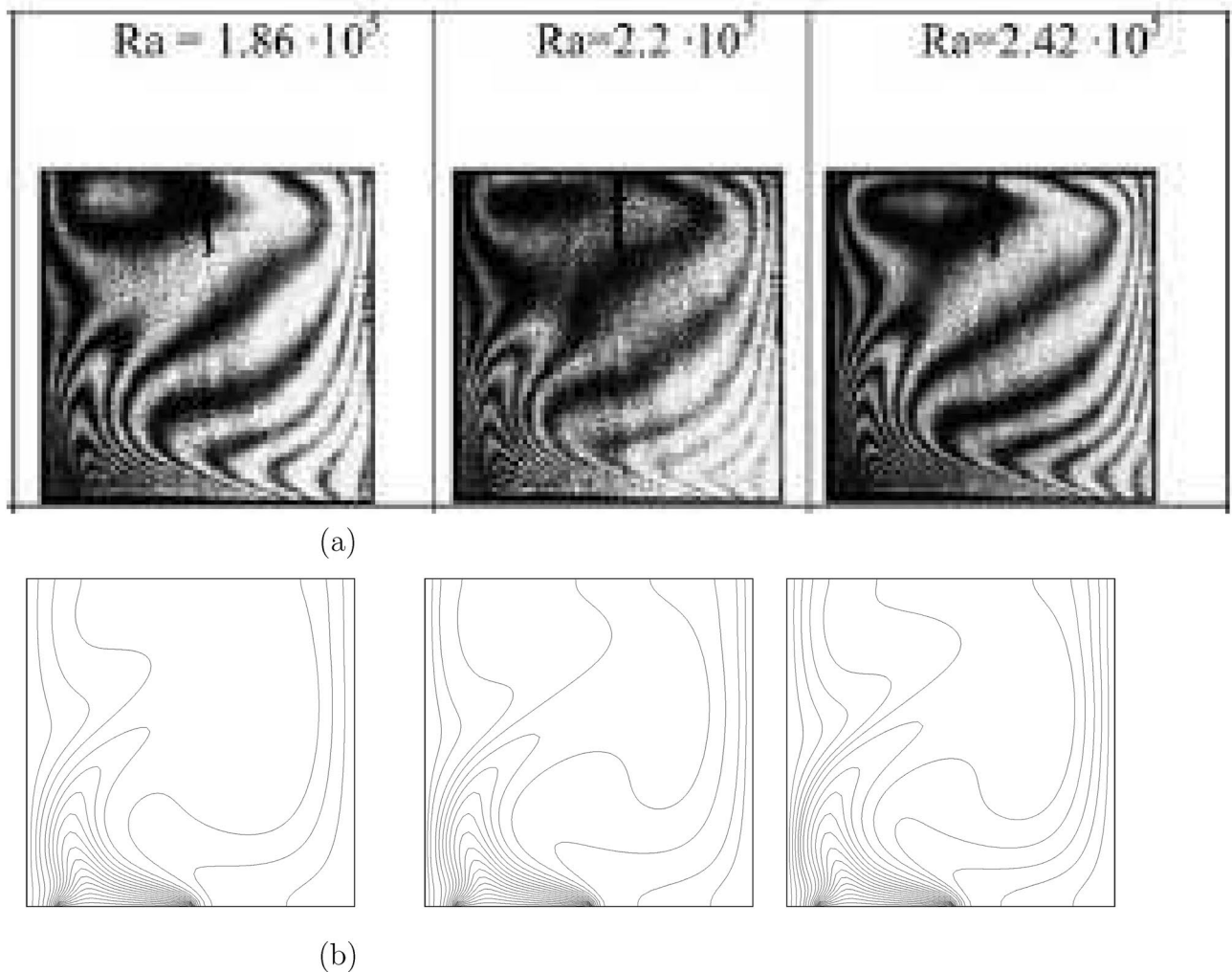


Fig. 7. Comparison of isotherms at different Ra and $\delta = 0.3$: (a) experimental results of Corvaro and Paroncini⁷¹ and (b) Present study.

We have also reproduced the problem investigated by Sompong et al.⁶⁹ inside an vertical wavy porous enclosure, as depicted in Fig. 5, and achieved excellent agreement.

A further validation involved a comparative study with Ma et al.'s work⁷⁰, specifically exploring parameters such as $Ra = 10^5$, $Ha = 20$, $Pr = 6.2$, $\phi = 0.05$ and $AR = 0.6$. Fig. 6 visually presents this analysis, showcasing flow and energy distributions inside a U-shaped cabinet. The compelling agreement observed between our outcomes and those in Ma et al.'s study underscores the code's proficiency in faithfully capturing flow and temperature distributions.

Fig. 7 provides a comparison of thermal distributions between our results and experimental results⁷¹ and obtained vigorous agreements between experimental data and our simulations.

Additionally, within Figure 8, we have reproduced the outcomes of entropy generation as investigated by Ilis et al.⁷². The confirmation underscores a substantial alignment between the findings of Ilis et al. and our simulation results, underscoring the precision of our code in forecasting entropy generation patterns. Through these validation exercises and comparative assessments, we collectively substantiate the strength and trustworthiness of our proprietary computational code in modelling intricate scenarios of fluid dynamics.

Moreover, Table 5 provides a contrast in the ψ_{\min} values between the findings of Al-Amiri et al.⁶⁷ and the outcomes from our ongoing research. The tabular data accentuates the adeptness of our computing code, affirming its capability to produce results that align consistently with established literature.

In Table 6, we have compared the values of \overline{Nu} and \overline{Sh} for the problem investigated by Bettaibi et al.⁷³ using our commutating in-house code. These results further validate the reliability and precision of our code in capturing key fluid dynamics parameters.

Table 7 provides a comparison of \overline{Nu} for various ϕ values between Nada et al.⁷⁴ and our simulation. The agreement in these tabular results reaffirms the accuracy of our in-house code across varying parameters.

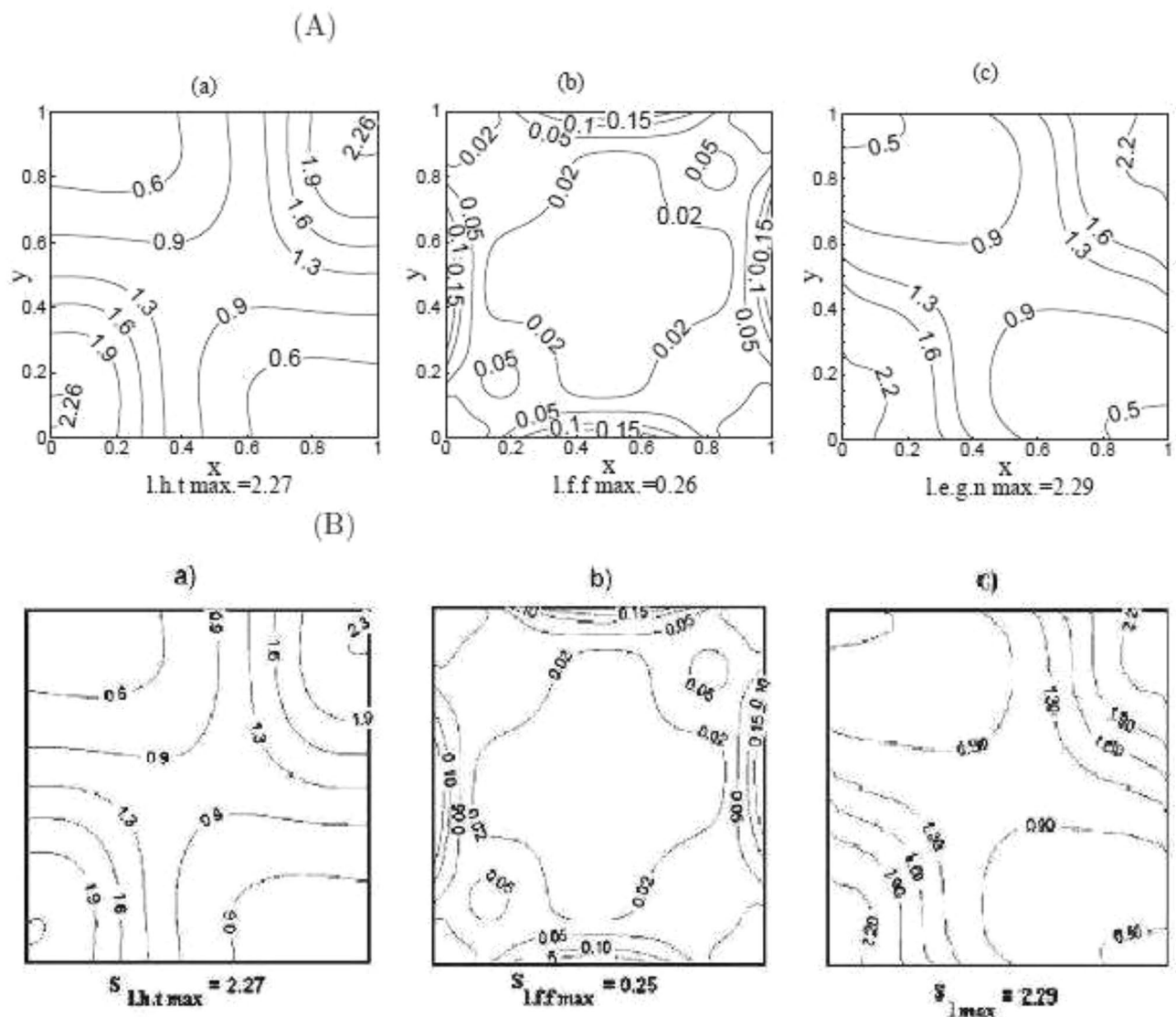


Fig. 8. Comparison of contours in (A) present work and (B) a numerical work of Ilis et al.⁷² for (a) local entropy generation due to heat transfer (b) local entropy generation due to fluid friction and (c) local entropy generation number for a cavity with a hot left wall and cold right wall with adiabatic top and bottom walls at $Ra = 10^3$ for $Pr = 0.7$.

N	-100	-50	-25	0	25	50	100
Present study	-0.0828	-0.0906	-0.0966	-0.1037	-0.1111	-0.1194	-0.1363
Al-Amiri et al. ⁶⁷	-0.0813	-0.0893	-0.0953	-0.1034	-0.1125	-0.1172	-0.1349

Table 5. Comparison of minimum values of streamfunction (ψ_{min}) for different values of N with $Re = 100$, $Ri = 0.01$, $Le = 1$ and $Pr = 1$ between Al-Amiri et al.⁶⁷ and present study.

Additionally, our results are cross-referenced with experimental observations by Ho et al.⁷⁵ and computational outcomes presented by Saghir et al.⁷⁶ in Table 8. The observed good agreement further attests to the capability of our code in accurately reproducing complex fluid dynamics scenarios.

Furthermore, in Table 9, a contrast is drawn between our values of \overline{Nu} and $|\psi|_{max}$ and those shown by Ghasemi et al.⁷⁷ across different Ha values. The consistency observed between results of⁷⁷ and our findings underscores the precision and dependability of our proprietary code.

In summary, the exhaustive validations and comparative assessments illustrated in the presented tables and figures collectively validate the precision, dependability, and adaptability of our proprietary code. Its consistent

N	\overline{Nu}		\overline{Sh}	
	Present study	Bettaibi et al. ⁷³	Present study	Bettaibi et al. ⁷³
-20	1.366	1.366	1.367	1.366
0	2.316	2.401	2.316	2.401
20	3.240	3.477	3.240	3.477

Table 6. Comparison of average Nusselt and Sherwood numbers at the hot bottom wall between the Bettaibi et al.⁷³ and present study for $Gr = 100$, $Re = 100$, $Pr = 1$ and $Le = 1$.

	$\phi = 0.0$	$\phi = 0.02$	$\phi = 0.05$	$\phi = 0.07$	$\phi = 1.0$
Nada et al. ⁷⁴	1.325	1.375	1.453	1.507	1.594
Present study	1.346	1.396	1.473	1.526	1.611

Table 7. Comparison of the average Nusselt numbers at top wall for different values of ϕ with $Gr = 100$ and $Ri = 5$ between Nada et al.⁷⁴ and present study.

Ha		$\phi = 0.0$		$\phi = 0.02$		$\phi = 0.04$	
		⁷⁷	Present	⁷⁷	Present	⁷⁷	Present
0	\overline{Nu}	4.738	4.712	4.820	4.793	4.896	4.868
	$ \psi _{max}$	11.053	11.323	11.313	11.583	11.561	11.832
30	\overline{Nu}	3.150	3.128	3.138	3.115	3.124	3.100
	$ \psi _{max}$	5.710	5.831	5.682	5.796	5.642	5.751
60	\overline{Nu}	1.851	1.837	1.831	1.817	1.815	1.802
	$ \psi _{max}$	2.633	2.663	2.534	2.534	2.415	2.448

Table 8. Comparison of average Nusselt number (\overline{Nu}) and $|\psi|_{max}$ among the present solution and Ghasemi et al.⁷⁷ for Al_2O_3 -water nanofluid at various Ha and with $Ra = 10^5$.

\overline{Nu}	$\phi = 1\%$	$\phi = 2\%$	$\phi = 3\%$
	$Ra_{nf} = 7.74547 \times 10^7$	$Ra_{nf} = 6.675118 \times 10^7$	$Ra_{nf} = 5.6020687 \times 10^7$
	$Pr_{nf} = 7.0659$	$Pr_{nf} = 7.3593$	$Pr_{nf} = 7.8353$
Exp ⁷⁵	32.2037	31.0905	29.0769
FEM-2D ⁷⁶	31.8633	31.6085	28.2160
FEM-3D ⁷⁶	32.7829	32.1833	31.3692
FDM-2D ⁷⁶	30.6570	30.5030	30.2050
LBM-2D ⁷⁶	30.0010	29.8370	29.6180
Present result	32.0521	31.2089	30.1379

Table 9. Comparison of \overline{Nu} between the experimental results, various numerical techniques and the present work for various ϕ , Ra_{nf} and Pr_{nf} .

delivery of accurate results across a diverse range of scenarios underscores its effectiveness in computational simulations.

In Table 10, we have summarized the grid sensitivity results for three different grid resolutions: 31×31 , 61×61 , and 121×121 . The results indicate that the 61×61 grid yields accurate and reliable outcomes for the considered problem.

Results and discussion

In this section, we analyze and present the outcomes from our study, offering a detailed demonstration of their physical significance. The computed outcomes are shown through visualizations of streamlines, isotherms, iso-concentrations, \overline{Nu} and \overline{Sh} , offering a comprehensive portrayal of thermosolutal phenomena under various physical parameters. This comprehensive exploration aims to contribute to a deeper understanding of the complex dynamics within the porous wavy cabinet loaded with a radiative hybrid nanofluid.

	Grids	Max $ \psi $	\overline{Nu}	\overline{Sh}
Case-1	31 × 31	0.414	14.816	6.393
	61 × 61	0.417	17.140	7.314
	121 × 121	0.418	17.142	7.315
Case-2	31 × 31	0.258	7.421	3.170
	61 × 61	0.253	8.584	3.629
	121 × 121	0.250	8.589	3.630
Case-3	31 × 31	0.374	5.391	2.899
	61 × 61	0.371	5.376	2.955
	121 × 121	0.370	5.372	2.958

Table 10. Grid independence study of the problem for Max $|\psi|$, \overline{Nu} and \overline{Sh} on the grids at $\phi_{hnp} = 0.04$, $m = 3.0$, $Ra = 10^5$, $Da = 10^{-4}$, $Ha = 25$, $Le = 5$, $N = 1$ and $Rd = 1$.

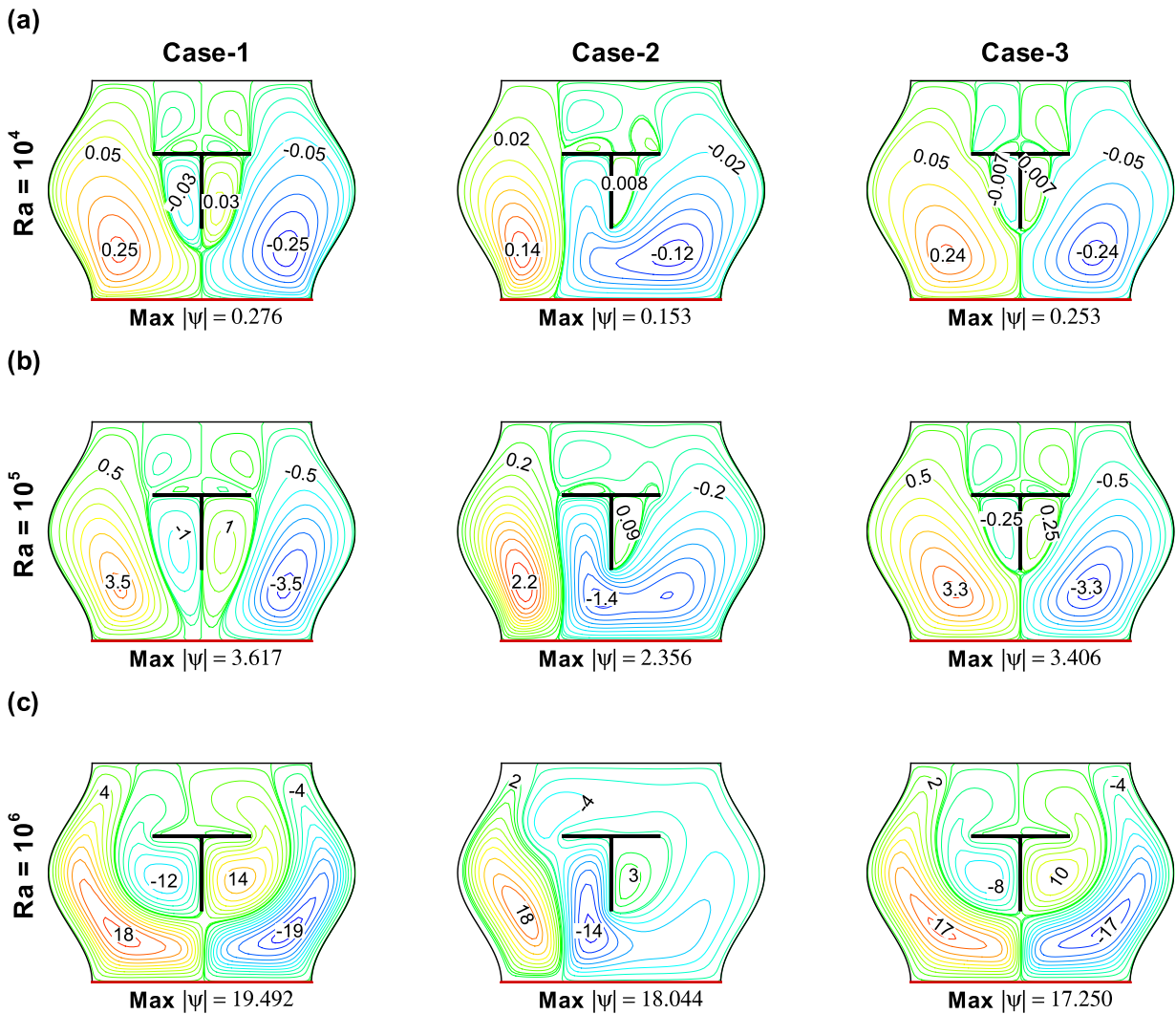


Fig. 9. Streamlines representing the fluid flow path within the baffled enclosure for different cases and Rayleigh number (Ra) with $\phi_{hnp} = 0.04$, $Ha = 25$, $Le = 1$, $Da = 10^{-3}$, $N = 1$ and $Rd = 1$. Max $|\psi|$ represents the maximum value of streamfunction.

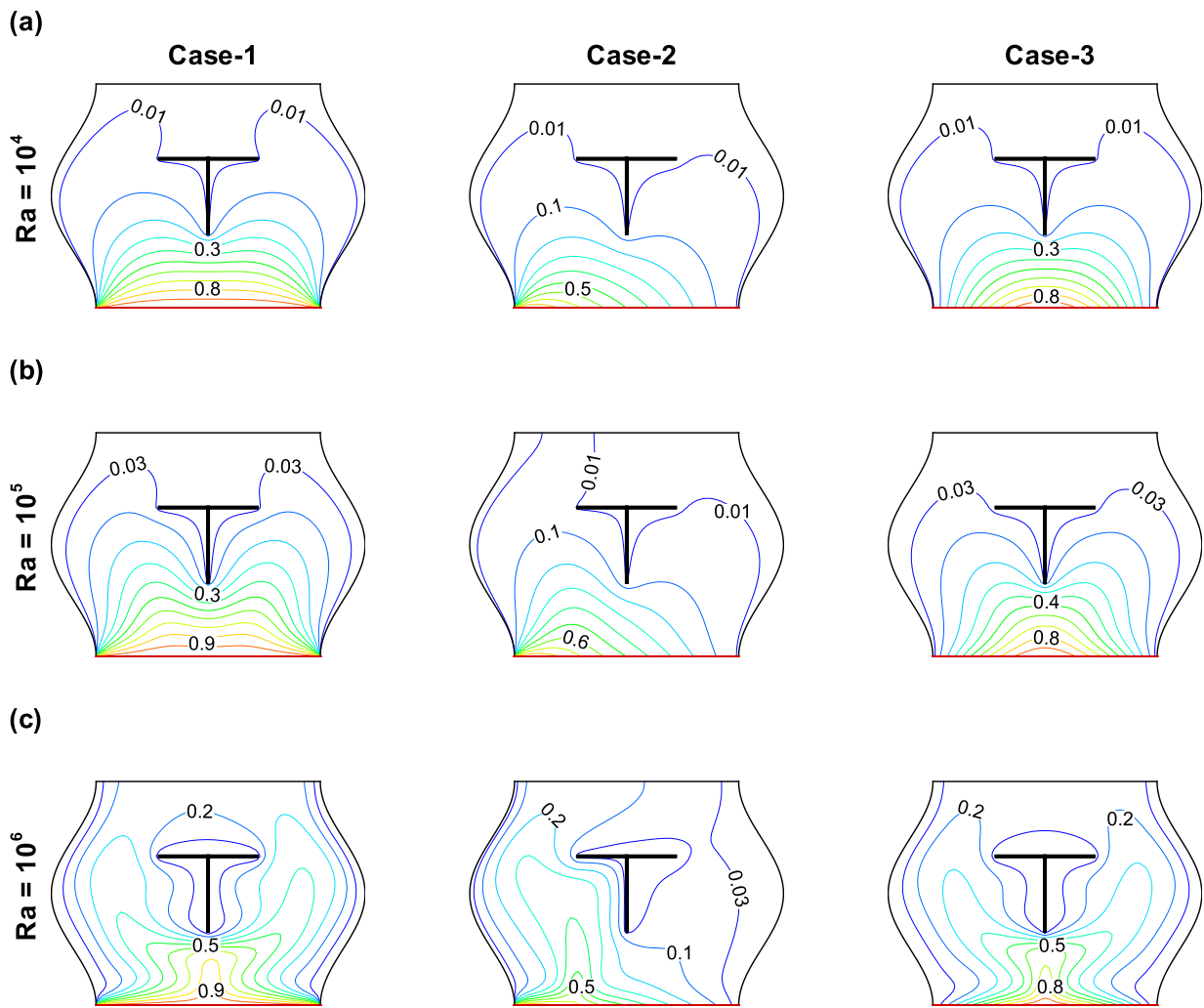


Fig. 10. Isotherms representing the heat flow path within the baffled enclosure for different cases and Rayleigh number (Ra) with $\phi_{hnp} = 0.04$, $Ha = 25$, $Le = 1$, $Da = 10^{-3}$, $N = 1$ and $Rd = 1$.

In Fig. 9, we delve into a comprehensive examination of how the Rayleigh number (Ra) intricately influences the behavior of a hybrid nanoliquid inside a wavy cabinet containing a T-shaped baffle under various heating strategies. The streamline contours for lower value Ra number are depicted in Figure 9(a), revealing a multicellular flow inside the porous cavity for all cases. In Case-1 (uniform heating) and Case-3 (non-uniform heating), two symmetric primary eddies form near the heated border. Conversely, Case-2 (linear heating) displays two asymmetrical primary vortices, with the left eddy occupying a smaller portion of the cavity due to linear heating being applied on the lower border. Secondary eddies also emerge and attach to the T-shaped cold baffle in all three cases. The warm fluid rises from the bottom of the cavity, moves toward the vertical sidewalls, and is deflected by the attached baffle, resulting in a total of six eddies inside the system. As Ra increases, the buoyancy forces become more pronounced, strengthening these primary circulations. Secondary eddies merge for higher Ra in all cases, and the magnitudes of the stream function increase with Ra . Specifically, modifying Ra from 10^4 to 10^6 results in a significant increase in $\text{Max}|\psi|$: 6962.31% for Case-1, 11693.46% for Case-2 and 6718.18% for Case-3. The corresponding isotherm lines in Fig. 10 offer insights into the thermal landscape. The warm fluid rises from the bottom of the cavity, moves toward the vertical sidewalls, and the adiabatic top surface redirects this flow, causing temperature lines to congest near the lower border. Steep energy gradients are observed, with higher temperature gradients near the hot lower border. The distinct temperature distributions for different heating strategies (Case-1, Case-2 and Case-3) are a result of the applied heating strategies. For example, Case-1 exhibits higher temperature at the bottom due to uniform heating, while Case-2 shows elevated temperatures on the left of the bottom border due to linear heating. Case-3, with non-uniform heating, displays higher temperatures at the midpoint of the bottom border. The T-shaped baffle plays a crucial role in reducing the expanse of the hot zone by obstructing and diverting the energy distribution within the enclosure. This reduction is a manifestation of the baffle's ability to alter the flow patterns and enhance thermal mixing. Figure 11 illustrates the species concentration profiles for $Le = 1$, revealing a strong correlation with the thermal

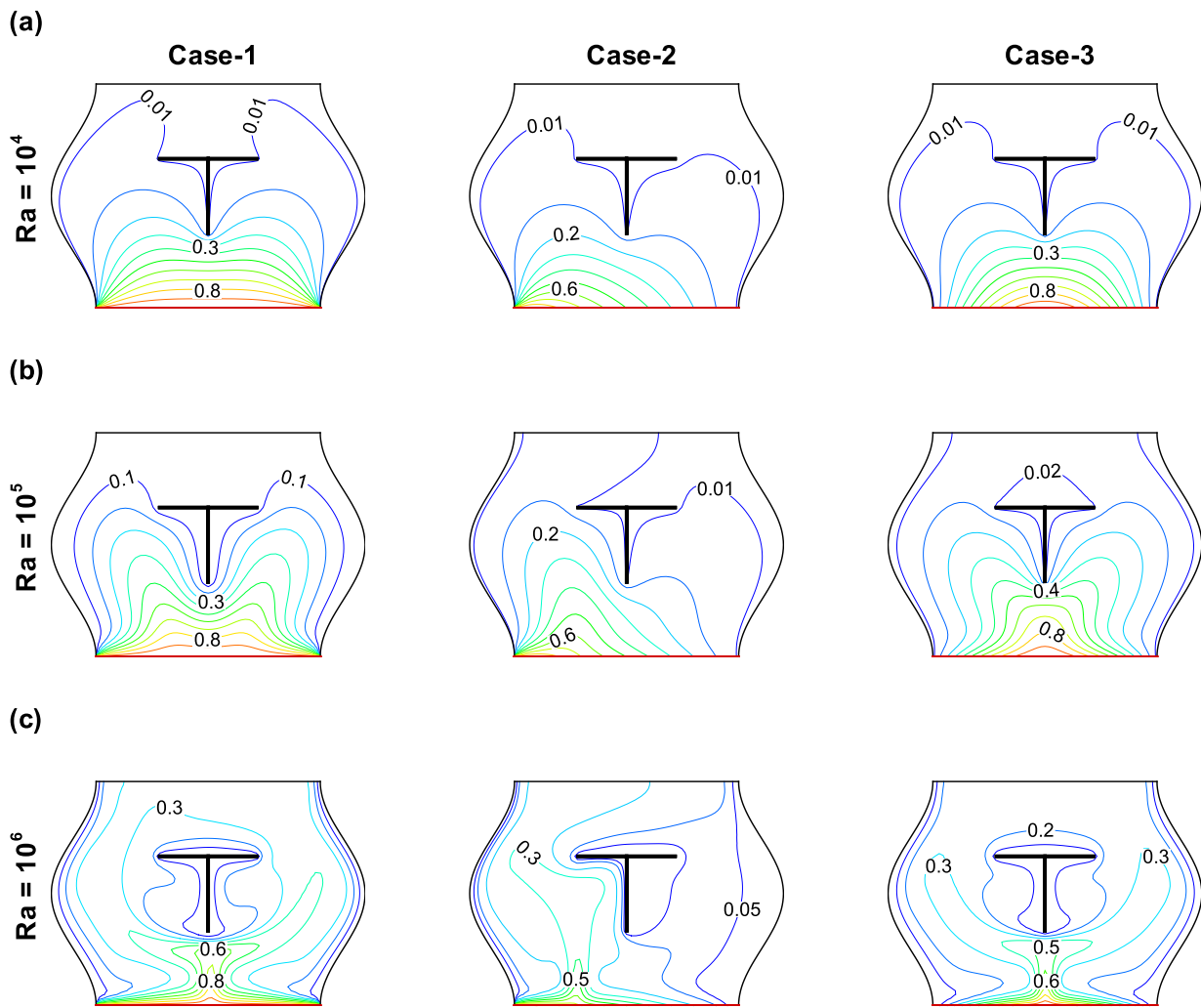


Fig. 11. Iso-solutal lines representing the mass (species) flow path within the baffled enclosure for different cases and Rayleigh number (Ra) with $\phi_{hnp} = 0.04$, $Ha = 25$, $Le = 1$, $Da = 10^{-3}$, $N = 1$ and $Rd = 1$.

distribution depicted in Fig. 10. This alignment arises due to the comparable diffusivities of heat and solute within the system, leading to analogous transport characteristics. The intricate coupling between flow topology, thermal convection, and species transport is governed by the imposed heating strategies and the obstructive influence of the T-shaped baffle, which modulates convective currents and diffusion pathways, thereby shaping the overall thermosolutal distribution.

In Fig. 12, we explore the effect of the Darcy number (Da) on flow distributions within the enclosure. For lower Da values, a multicellular flow pattern is observed, distinguished by the arrangement of symmetric eddies for Case-1 and Case-3. In Case-2, with linear heating of the lower border, two weak asymmetric primary eddies are generated. This behavior is attributed to the dominance of viscous forces over buoyancy forces at low Da . As Da increases, the magnitudes of the stream function in every case also increase. The change in Da from 10^{-4} to 10^{-2} results in a significant boost in $\text{Max}|\psi|$: 6962.31% for Case-1, 11693.46% for Case-2 and 6718.18% for Case-3. Fig. 13 presents the corresponding thermal distribution for various Da within the system. Isotherms are congested near the heated border, indicating a steep thermal gradient near the hot border. The presence of steep temperature gradients near the heated boundary is evident, signifying regions of intense thermal transport. Notably, the energy concentration varies across different heating configurations: in Case-1, maximum thermal energy accumulates along the heated boundary of the chamber; in Case-2, it is concentrated on the left segment of the lower wall; whereas in Case-3, the peak temperature region is localized at the central portion of the lower boundary. The introduction of the T-shaped fin significantly alters the thermal field by acting as a thermal barrier, constraining heat propagation, and redistributing convective currents, thereby reducing the spatial extent of the high-temperature region within the chamber.

In Fig. 14, solutal lines are presented, providing insights into solute dispersion inside the enclosure. It is observed that the species lines are more crowded compared to the energy lines. The observed higher species transfer than energy transport inside the system signifies the complex interplay between mass and heat transfer

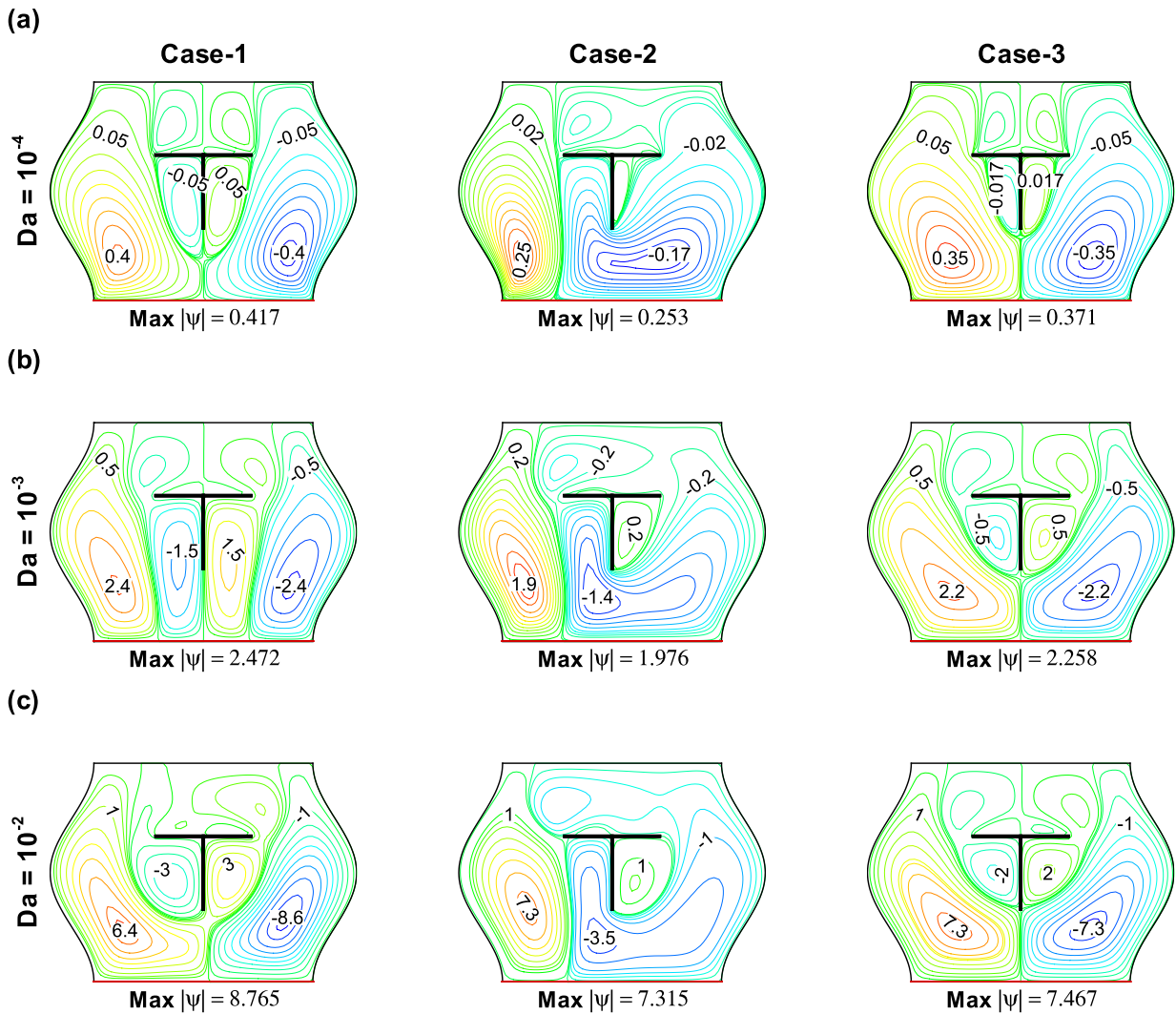


Fig. 12. Streamlines representing the fluid flow path within the baffled enclosure for different cases and Darcy number (Da) with $\phi_{hnp} = 0.04$, $Ra = 10^5$, $Ha = 25$, $Le = 5$, $N = 1$ and $Rd = 1$. $\text{Max}|\psi|$ represents the maximum value of streamfunction.

phenomena. Thus, the observed flow patterns, thermal distributions, and solute dispersion are intricately linked to the variation in Da . The dominance of viscous forces, the influence of heating strategies, and the role of the T-shaped fin collectively contribute to the thermal behavior and complex fluid dynamics within the wavy enclosure.

In Fig. 15, we delve into the nuanced interplay between the Lewis number (Le) and various facets of the system's behavior, exploring how Le influences the flow topology, thermal characteristics, and solute transport inside the container. The observed multi-cellular flow pattern within the container is characterized by two symmetric primary vortices. Additionally, for Case-1 and Case-3, four secondary cells intimately attach to the cold T-shaped fin, while Case-2 exhibits two primary eddies within the chamber along with a small secondary vortex attached to the fin. Notably, while Le does not significantly alter the flow structure inside the cavity, an increase in Le from 1 to 10 leads to a reduction in $\text{Max}|\psi|$ by 42.15% in Case-1, 50.19% in Case-2, and 47.45% in Case-3, indicating a diminishing convective flow intensity. The corresponding isotherm lines in Figure 16 visually narrate the temperature distribution within the enclosure. The clustering of isothermal contours near the heated boundary signifies intense convective heat transport in this region, driven by buoyancy-induced flow. The interaction between the thermal field and the T-shaped cold fin introduces a complex interplay between geometric constraints and thermally induced fluid motion. Notably, the thermal gradient exhibits a higher magnitude in the lower half of the enclosure compared to the upper region, indicating asymmetric thermal diffusion influenced by convective currents. Interestingly, the Lewis number (Le) exerts a negligible influence on the overall thermal distribution within the enclosure, suggesting that thermal transport remains primarily governed by convective and conductive mechanisms rather than species diffusivity. Fig. 17 presents solutal lines for different Le , revealing the presence of vigorous convective solutal transfer near the lower wall. As Le rises, a significant modification is found in concentration contours close to the lower wall. The species transport

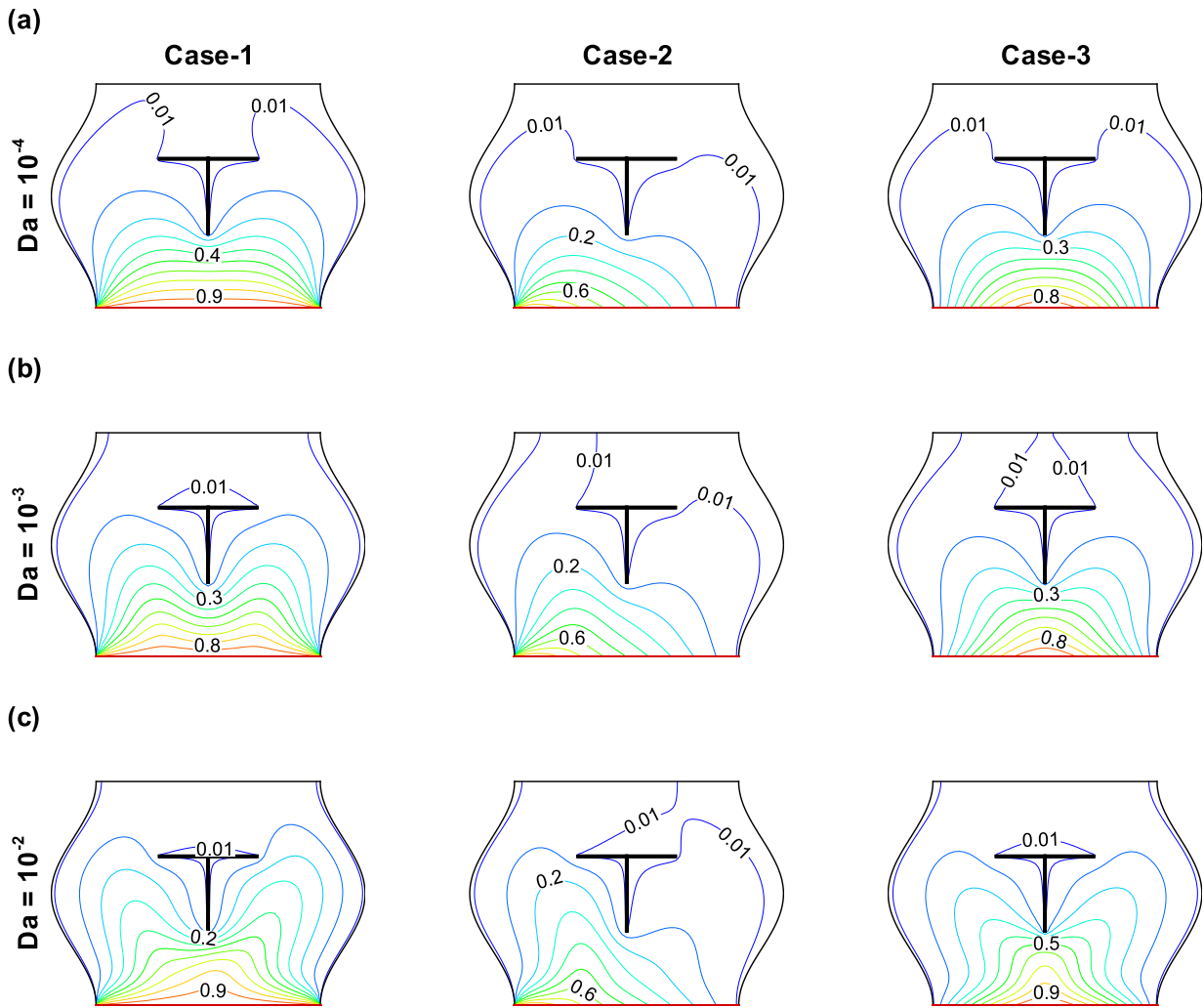


Fig. 13. Isotherms representing the heat flow path within the baffled enclosure for different cases and Darcy number (Da) with $\phi_{hnp} = 0.04$, $Ra = 10^5$, $Ha = 25$, $Le = 5$, $N = 1$ and $Rd = 1$.

becomes higher compared to that of the energy inside the container. The interplay between thermal and solute dynamics underscores the complex nature of mass and heat transfer phenomena within the wavy enclosure.

Thermal assessment: Average Nusselt (\overline{Nu}) and Sherwood number (\overline{Sh}):

In Figure 18, we delve into an insightful exploration of the influence of varying nanoparticle volume fraction (ϕ_{hnp}) on \overline{Nu} and \overline{Sh} in three distinct cases, each characterized by $m = 3.0$, $Ra = 10^5$, $Da = 10^{-3}$, $Ha = 25$, $Le = 2$, $N = 1$ and $Rd = 1$. Throughout this analysis, we observe a consistent upward trajectory in \overline{Nu} as ϕ_{hnp} increases, which indicates improved energy transfer capability of nanofluids. Specifically, with an increase in ϕ_{hnp} from 0.0 to 0.04, \overline{Nu} experiences significant enhancements of 3.50%, 4.21%, and 1.18% in Case-1, Case-2 and Case-3, respectively. In contrast, the behavior of \overline{Sh} illustrates a contrasting downward trend with growing ϕ_{hnp} . The decline in \overline{Sh} is noteworthy, with respective reductions of 7.10%, 5.84% and 6.72% in Case-1, Case-2, and Case-3 when ϕ_{hnp} is elevated from 0.0 to 0.04. Additionally, it is noteworthy that the optimal conditions for both energy and species transfer occur at $\phi_{hnp} = 0.04$. This particular nanoparticle volume fraction yields the maximum energy transfer efficiency and the minimum species transfer, indicating a delicate balance between the two processes. Among the three cases considered, Case-1, characterized by uniform heating, emerges with the maximum mean Nusselt number. This is followed by Case-2 with linear heating, and Case-3 with non-uniform heating, for all values of nanoparticle volume fraction (ϕ_{hnp}). This ranking implies that the configuration featuring uniform heating (Case-1) provides the most efficient species and energy transfer dynamics in this study.

In Figure 19, we display a comprehensive examination of the variations in \overline{Nu} and \overline{Sh} for different Rayleigh numbers (Ra) across all three cases, where $m = 3.0$, $\phi_{hnp} = 0.04$, $Ha = 25$, $Da = 10^{-3}$, $N = 1$, $Le = 1$ and $Rd = 1$. The investigation reveals intriguing insights into the solutal and energy transfer characteristics as Ra undergoes systematic increments. As Ra increases, both \overline{Nu} and \overline{Sh} demonstrate noteworthy enhancements.

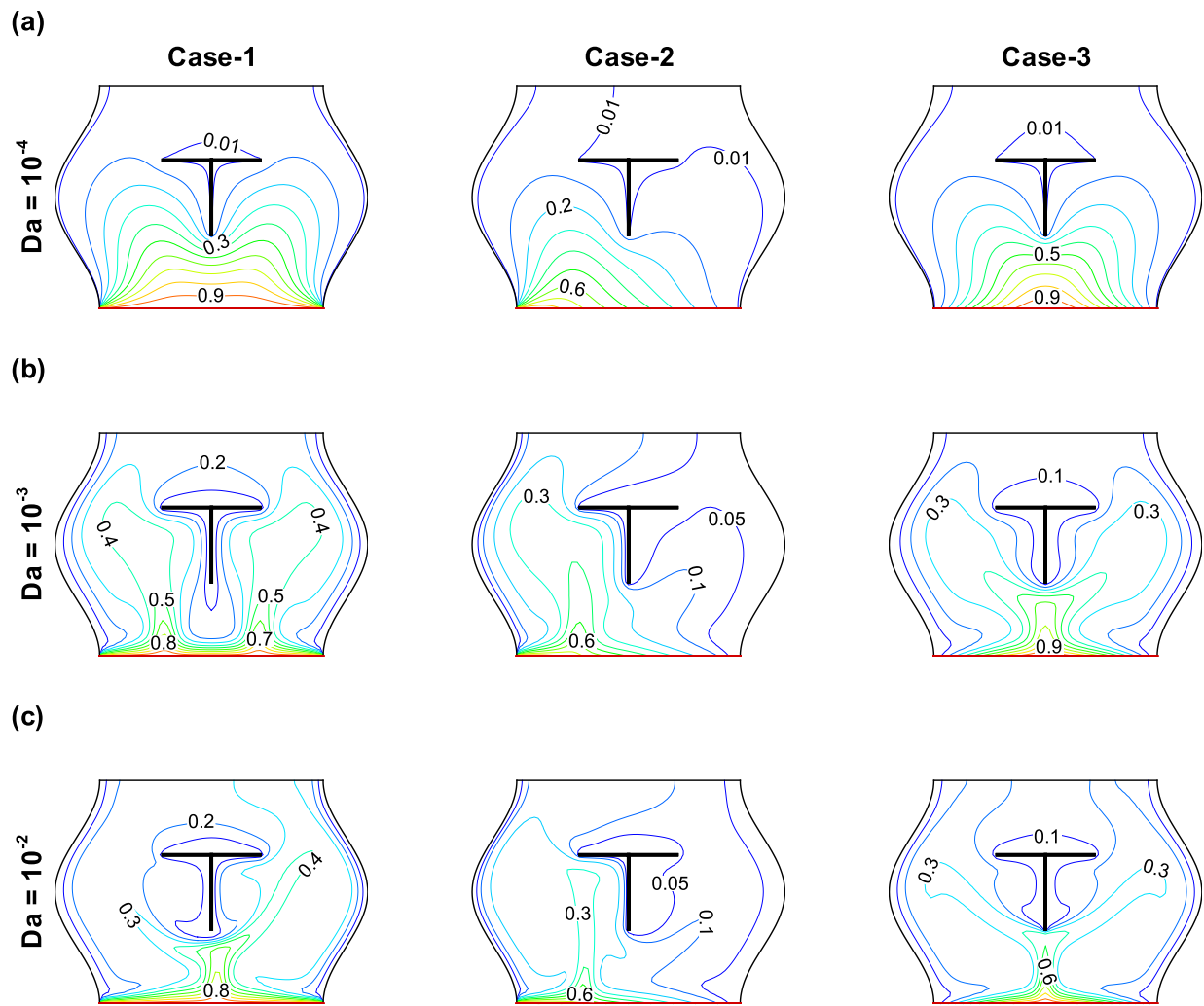


Fig. 14. Iso-solutal lines representing the mass (species) flow path within the baffled enclosure for different cases and Darcy number (Da) with $\phi_{hnp} = 0.04$, $Ra = 10^5$, $Ha = 25$, $Le = 5$, $N = 1$ and $Rd = 1$.

Specifically, with a transition from $Ra = 10^4$ to $Ra = 10^6$, \overline{Nu} experiences substantial improvements of 65.16%, 66.69% and an impressive 207.11% in Case-1, Case-2 and Case-3, respectively. The results indicate that an increase in the Rayleigh number (Ra) enhances thermal buoyancy-driven convection, leading to significantly more efficient heat transport across all considered cases. Concurrently, the mass transfer efficiency, characterized by the average Sherwood number (\overline{Sh}), exhibits substantial augmentation with increasing Ra . Specifically, a variation in Ra from 10^4 to 10^6 yields enhancements of 131.50%, 132.38%, and an exceptional 385.60% in Case-1, Case-2, and Case-3, respectively. This highlights the pivotal role of thermal buoyancy in modulating solutal transport mechanisms within the nanofluid medium. Moreover, it is particularly noteworthy that the maximal rates of both heat and species transport are attained at $Ra = 10^6$ in Case-1, suggests that, under uniform heating conditions, the upper bound of Ra corresponds to the most favorable regime for coupled thermosolutal convection.

In Figure 20, we conduct a thorough exploration of the variations in \overline{Nu} and \overline{Sh} with different Darcy number (Da). As Da increases, both \overline{Nu} and \overline{Sh} consistently show improvements. Specifically, transitioning from $Da = 10^{-4}$ to $Da = 10^{-2}$ yields enhancements of 14.80% and 11.40% in Case-1, 13.80% and a substantial 123.28% in Case-2 and 61.79% and an impressive 258.95% in Case-3, respectively. The observed upgrades in \overline{Nu} and \overline{Sh} with increasing Da can be attributed to the influence of permeability on fluid flow within the porous medium. As Da increases, the flow resistance decreases, leading to enhanced convective species and energy transfer. The more pronounced impact on \overline{Sh} in Case-3 suggests that the non-uniform heating configuration is particularly sensitive to changes in Da .

Figure 21 visually presents the variations in \overline{Nu} and \overline{Sh} with different Hartmann numbers (Ha), showcasing significant reductions in both parameters as Ha increases. The key observation is the pronounced restraining effect exerted by the Lorentz force on the fluid's motion inside the domain, resulting in noteworthy consequences

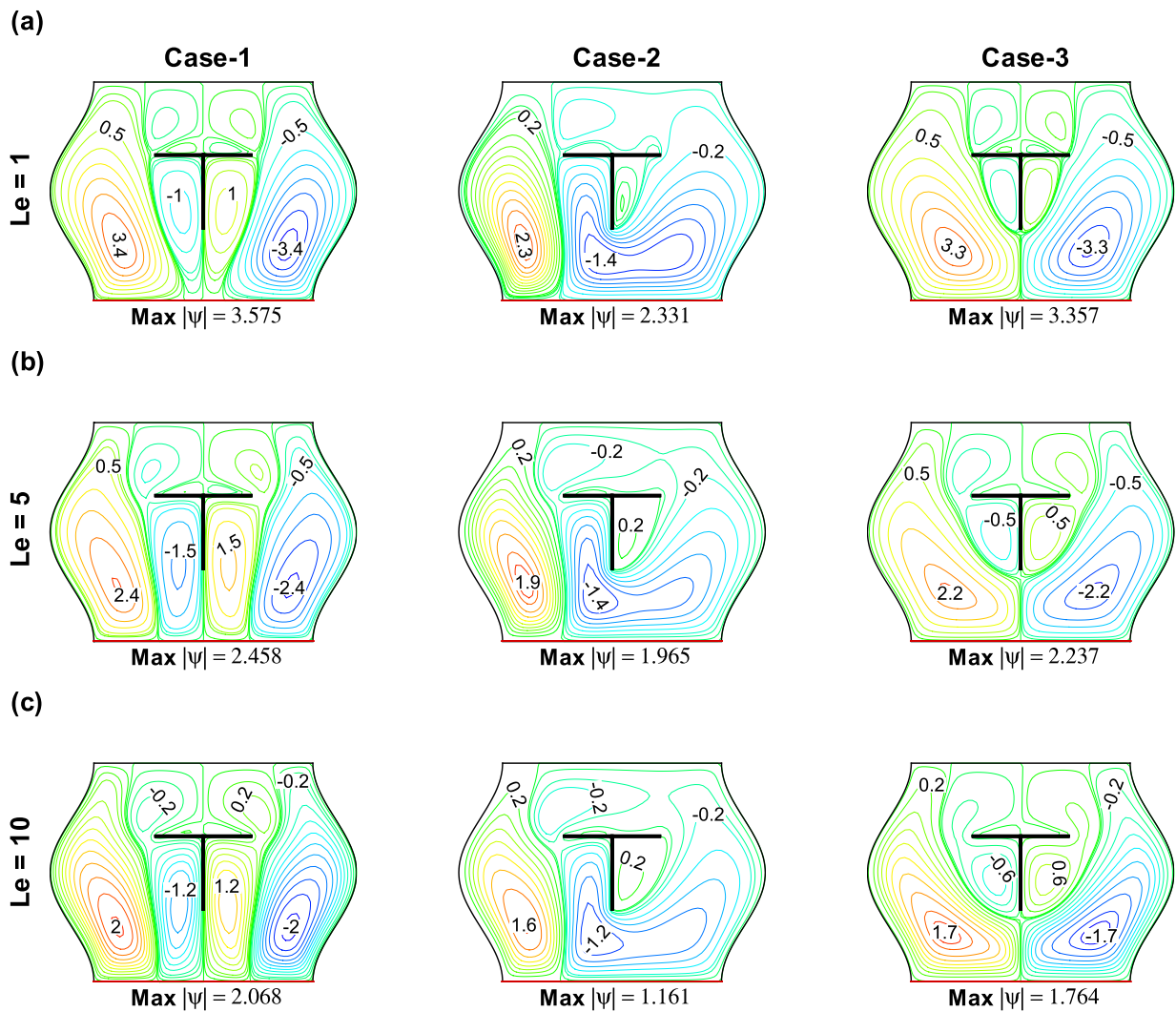


Fig. 15. Streamlines representing the fluid flow path within the baffled enclosure for different cases and Lewis number (Le) with $Ra = 10^5$, $\phi_{hnp} = 0.04$, $Da = 10^{-3}$, $Ha = 30$, $N = 1$ and $Rd = 1$. $\text{Max}|\psi|$ represents the maximum value of streamfunction.

for species and energy transfer dynamics. It is crucial to underscore the role of the Lorentz force, produced by the magnetic field, as it overwhelmingly diminishes thermosolutal transfer rates. This dominance of the Lorentz force becomes apparent in the substantial reductions observed in both \overline{Nu} and \overline{Sh} as Ha is increased. The restraining effect on fluid motion contributes to an intricate interplay between magnetic fields and convective transport processes. Specifically, at $Ha = 60$, \overline{Nu} and \overline{Sh} experience reductions of 0.65% and 1.94%, respectively, in Case-1. In Case-2, the reductions are slightly more pronounced, with \overline{Nu} diminishing by 0.82% and \overline{Sh} by 2.85%. Case-3 exhibits the most substantial reductions, with \overline{Nu} and \overline{Sh} diminishing by 4.53% and 9.48%, respectively, relative to their values at $Ha = 0$.

In Figure 22, we delve into a detailed investigation of the impacts of the buoyancy parameter (N) on thermal and species transfer, considering parameters such as $m = 3.0$, $\phi_{hnp} = 0.04$, $Ra = 10^5$, $Da = 10^{-3}$, $Le = 1$, $Ha = 25$ and $Rd = 1$. The significance of the buoyancy parameter, denoted as N , becomes evident as a key indicator of the complex interaction between buoyancy forces resulting from species and energy gradients inside a medium. This interaction significantly impacts the dynamics of energy and species transfer. Our exploration unveils noteworthy patterns as the buoyancy parameter N experiences changes. With increasing values of N , both \overline{Nu} and \overline{Sh} exhibit consistent and significant improvements. Specifically, changing from $N = 0$ to $N = 10$, we notice remarkable enhancements of 58.22% and 120.66% for Case-1, 36.75% and 86.29% for Case-2, and 110.71% and 214.44% for Case-3 in \overline{Nu} and \overline{Sh} , respectively. The buoyancy parameter N acts as a quantifiable measure of the impact of buoyancy forces on the fluid motion and transport processes. The observed improvements in both \overline{Nu} and \overline{Sh} underscore the pivotal role of buoyancy in enhancing convective heat and mass transfer. Higher values of N indicate stronger buoyancy effects, leading to more efficient transport of heat and species within the nanofluid.

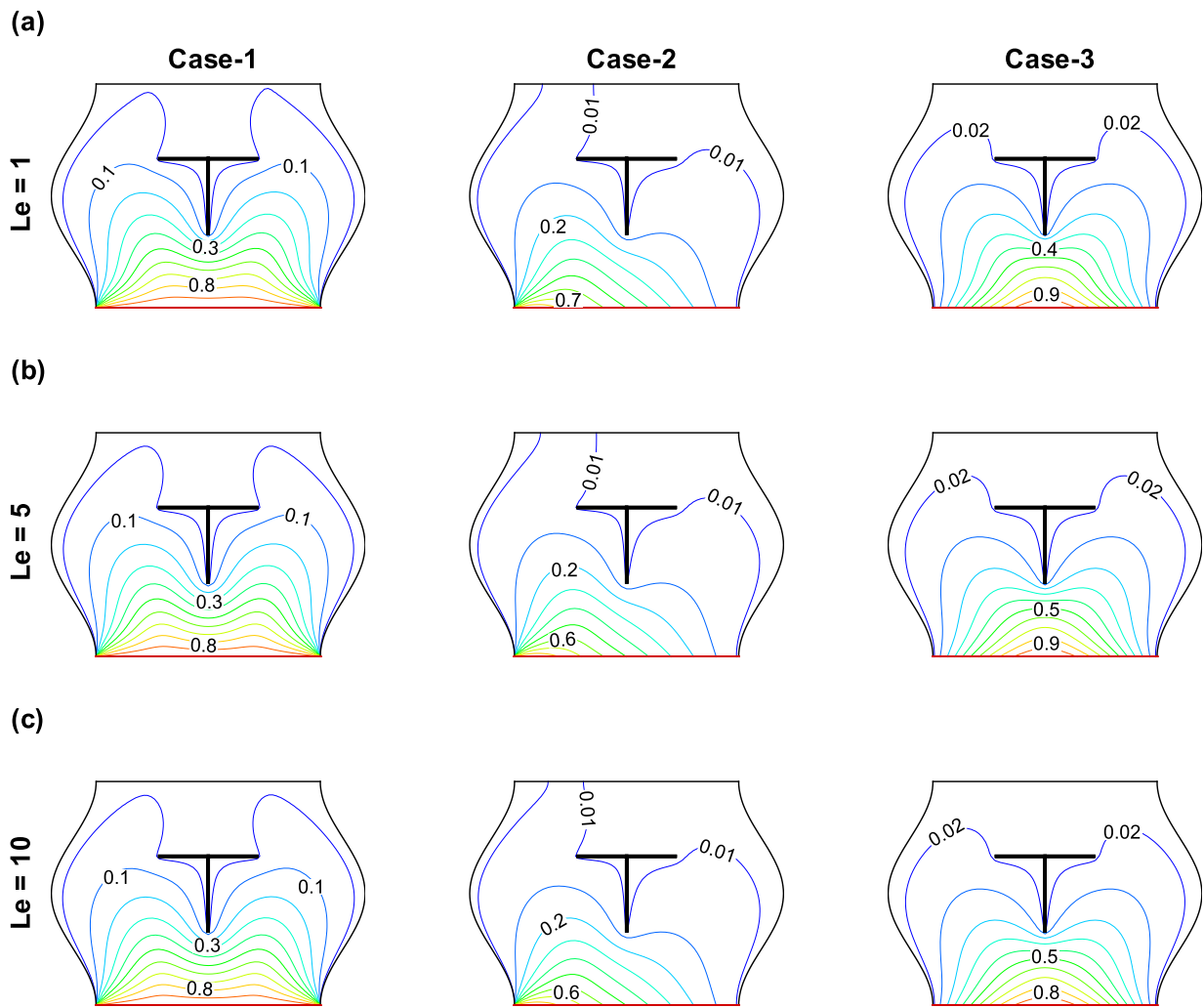


Fig. 16. Isotherms representing the heat flow path within the baffled enclosure for different cases and Lewis number (Le) with $Ra = 10^5$, $\phi_{hnp} = 0.04$, $Da = 10^{-3}$, $Ha = 30$, $N = 1$ and $Rd = 1$.

Figure 23 illustrates the influences of the Lewis number (Le) on \overline{Nu} and \overline{Sh} for conditions characterized by $Ra = 10^5$, $\phi_{hnp} = 0.04$, $m = 3.0$, $Da = 10^{-3}$, $Ha = 30$, $N = 1$ and $Rd = 1$. The noticed patterns in species and energy transfer present intriguing insights into the intricate balance of diffusive processes within the nanofluid system. As the Lewis number (Le) increases, a distinctive phenomenon unfolds: energy transfer diminishes while solutal transfer is enhanced. This behavior is rooted in the fundamental physics of diffusive processes, where modifications in Le directly influence the competition between thermal and solutal transport. Specifically, with a change in Le from 1 to 10, we observe a reduction in \overline{Nu} by up to 1.30% in Case-1, 0.96% in Case-2, and a more pronounced 9.25% in Case-3. This reduction in \overline{Nu} indicates that as Le increases, thermal diffusion becomes less efficient, leading to a decrease in overall energy transfer rates. Conversely, \overline{Sh} experiences significant enhancements with increasing Le . The solutal transfer is boosted by 119.49%, 101.07%, and 166.32% in Case-1, Case-2 and Case-3, respectively, when transitioning from $Le = 1$ to $Le = 10$. This emphasizes that higher Lewis numbers favor solutal diffusion, resulting in more efficient solutal transport inside the nanofluid system.

In Figure 24, we explore the influence of the radiation parameter (Rd) on \overline{Nu} and \overline{Sh} for conditions characterized by $m = 3.0$, $Ra = 10^5$, $\phi_{hnp} = 0.04$, $Da = 10^{-3}$, $Ha = 25$, $N = 1$ and $Le = 1$. The observed trends highlight the significant effect of radiative heat transfer mechanisms on the species and energy transport dynamics within the nanofluid. As Rd increases, a distinct phenomenon unfolds: \overline{Nu} experiences remarkable enhancements, while \overline{Sh} undergoes reductions. This behavior underscores the crucial role played by radiative heat transfer mechanisms in modulating the overall performance of heat and mass transfer processes. Notably, as Rd increases from 1 to 10, \overline{Nu} undergoes substantial enhancements of up to 467.12% in Case-1, 470.98% in Case-2 and 387.78% in Case-3. This remarkable increase in \overline{Nu} suggests that radiative heat transfer becomes increasingly dominant, leading to more efficient thermal transport within the nanofluid. Conversely, \overline{Sh}

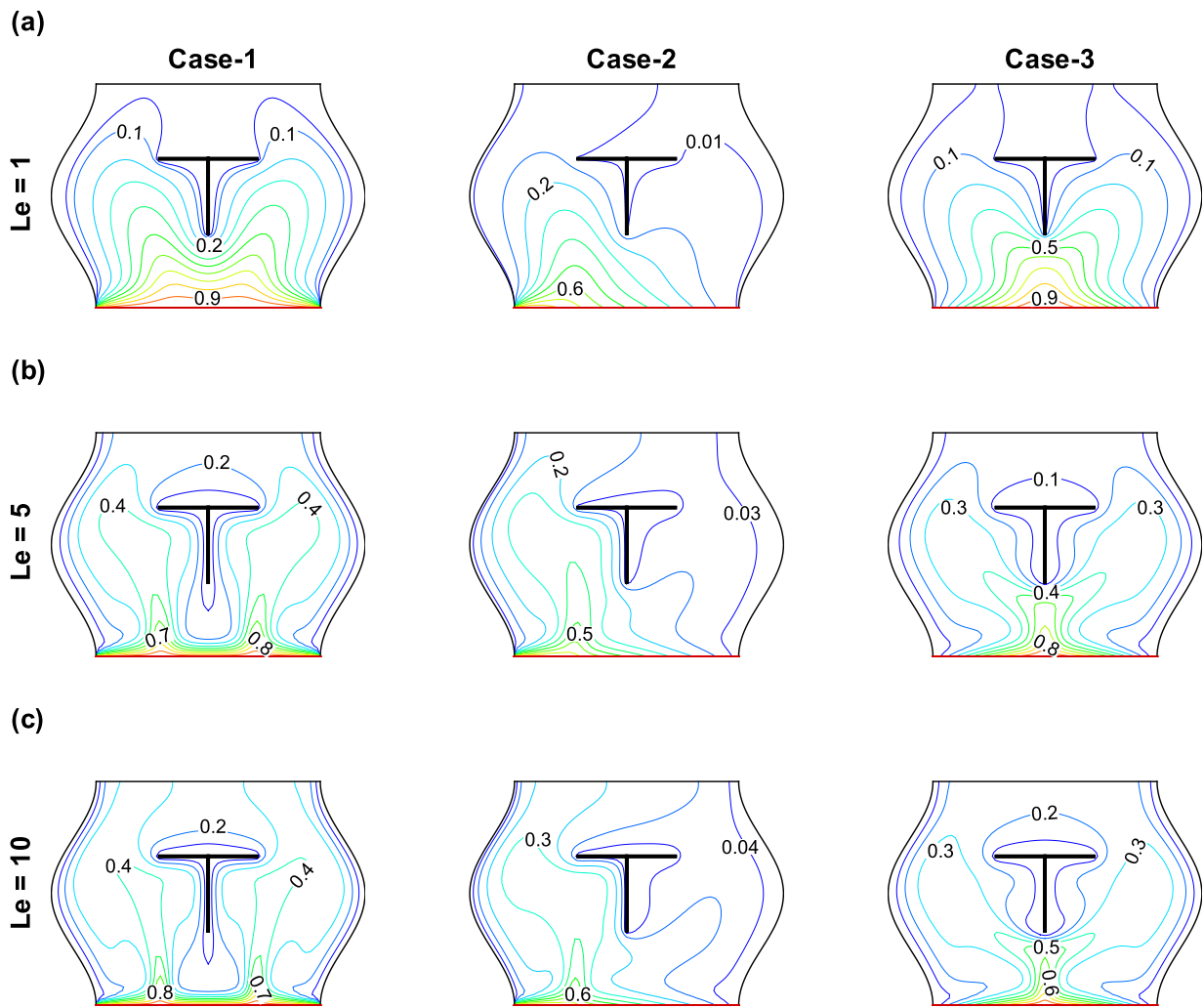


Fig. 17. Iso-solutal lines representing the mass (species) flow path within the baffled enclosure for different cases and Lewis number (Le) with $Ra = 10^5$, $\phi_{hnp} = 0.04$, $Da = 10^{-3}$, $Ha = 30$, $N = 1$ and $Rd = 1$.

experiences reductions with increasing Rd . The solutal transfer diminishes by 3.09%, 2.05%, and 6.07% in Case-1, Case-2 and Case-3, respectively, as Rd transitions from 1 to 10. This indicates that the dominance of radiative heat transfer mechanisms hinders solutal diffusion, resulting in a decrease in overall mass transfer efficiency. In a general sense, the optimum thermal performance is observed at $Rd = 10$ for Case-1.

Examining Figure 25 provides an in-depth analysis of how the nanoparticle shape factors (m) and solid volume fraction (ϕ_{hnp}) exert influence on \overline{Nu} and \overline{Sh} , under specific conditions: $Ra = 10^5$, $Da = 10^{-3}$, $Ha = 25$, $N = 1$ and $Le = 1$. The observed trends reveal intricate relationships between nanoparticle characteristics and thermosolutal transfer in the nanofluid. For fixed values of m , it is noted that energy transfer, represented by \overline{Nu} , improves while species transfer, represented by \overline{Sh} , diminishes. Similarly, for fixed ϕ_{hnp} , \overline{Nu} enriches, and \overline{Sh} reduces. These trends highlight the nuanced impact of both shape factors and solid volume fraction on the thermal and species transfer dynamics inside the nanofluid. Specifically, in Case-1, with $\phi_{hnp} = 0.04$, \overline{Nu} is upgraded by 3.50%, 4.60%, 6.31%, 7.71% and 12.21% with respect to $\phi_{hnp} = 0.0$ for $m = 3.0, 3.7, 4.8, 5.7, 8.6$, respectively. Simultaneously, \overline{Sh} is shortened by 7.10%, 7.15%, 7.32%, 7.44% and 7.84%, respectively. Parallel patterns are discernible in both Case-2 and Case-3. The attainment of optimal species and energy transfer is notably observed in the context of blade-shaped nanoparticles ($m = 8.6$).

Analysis of entropy generation

Table 11 and Figure 26 (a) showcases a discernible escalation in entropy production values as Ra experiences enhancement. This phenomenon finds its roots in the augmented rates of species and energy transport. The intensification of convective heat transfer with improving Ra leads to a concurrent elevation in entropy generation. Notably, the impact of mass transfer becomes increasingly evident, notably contributing to higher entropy production, particularly in cases such as E_{MT} and E_{MF} . A noteworthy observation is the attainment

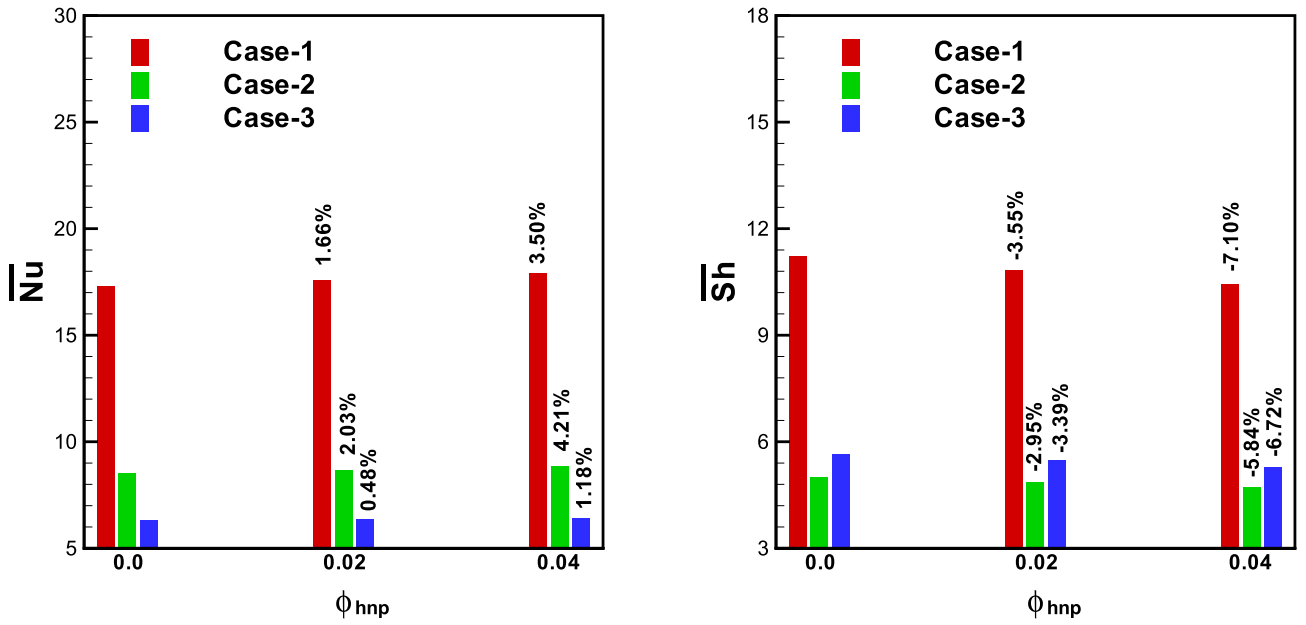


Fig. 18. The bar chart represents variation of average Nusselt number (\overline{Nu}) and average Sherwood number (\overline{Sh}) with solid volume fraction (ϕ_{hnp}) for different cases and $Ra = 10^5$, $Da = 10^{-3}$, $Ha = 25$, $Le = 2$, $N = 1$ and $Rd = 1$.

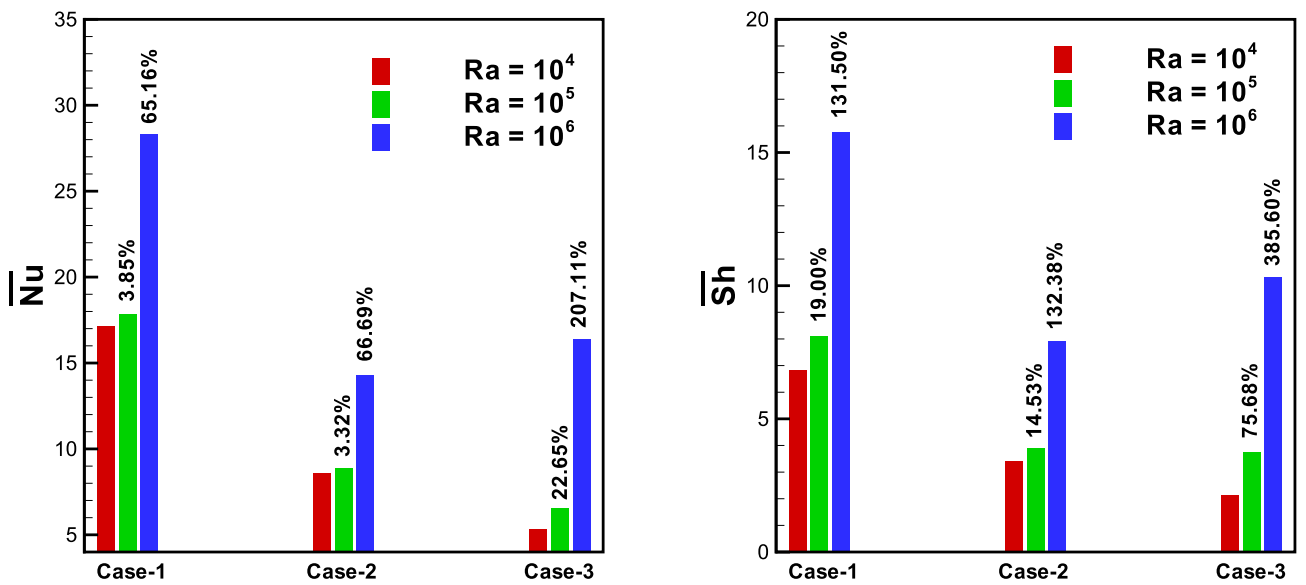


Fig. 19. The bar chart represents variation of average Nusselt number (\overline{Nu}) and average Sherwood number (\overline{Sh}) with Rayleigh number (Ra) for different cases and $\phi_{hnp} = 0.04$, $Ha = 25$, $Le = 1$, $Da = 10^{-3}$, $N = 1$ and $Rd = 1$.

of optimal values for entropy production metrics at $Ra = 10^6$, indicative of a delicate equilibrium between heightened species and energy transfer processes. Conversely, the diminishing trend observed in Be as Ra improves is explained by the prevalence of heat transfer effects. At lower Ra values, fluid friction effects are more pronounced, resulting in higher Be . However, with the ascent of Ra , the influence of heat transfer becomes more pronounced, causing a subsequent reduction in Be .

In Table 12, the influence of N on entropy productions and the Bejan number is unveiled. The observed increase in entropy production values as N enriches can be linked to heightened buoyancy-driven phenomena.

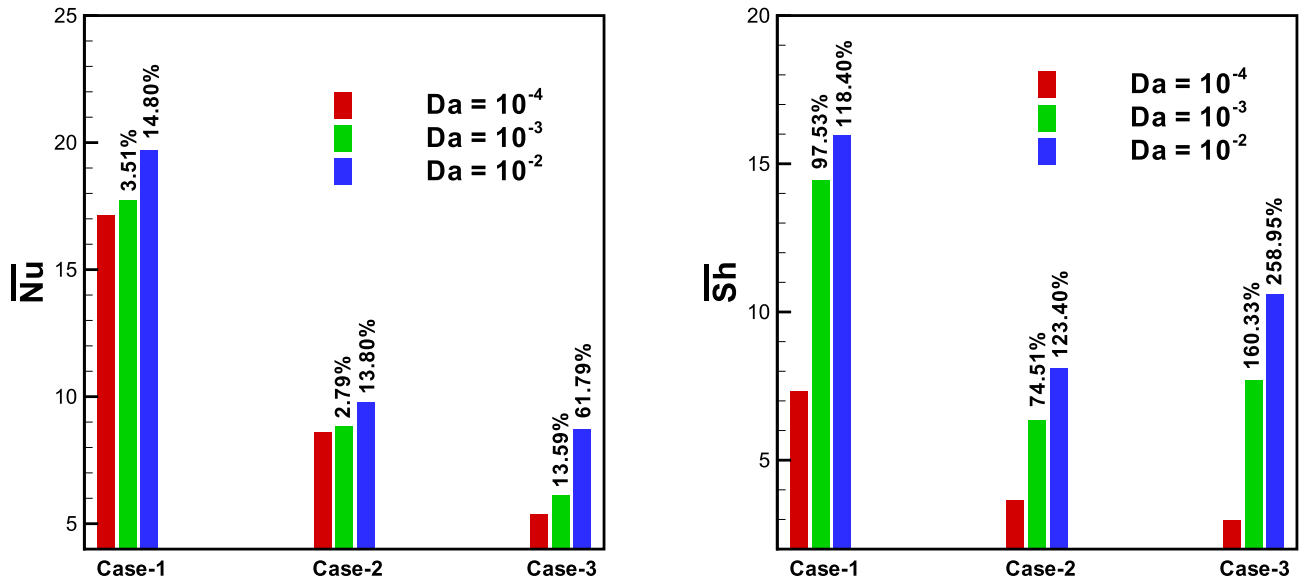


Fig. 20. The bar chart represents variation of average Nusselt number (\overline{Nu}) and average Sherwood number (\overline{Sh}) with Darcy number (Da) for different cases and $\phi_{hnp} = 0.04, Ra = 10^5, Ha = 25, Le = 5, N = 1$ and $Rd = 1$.

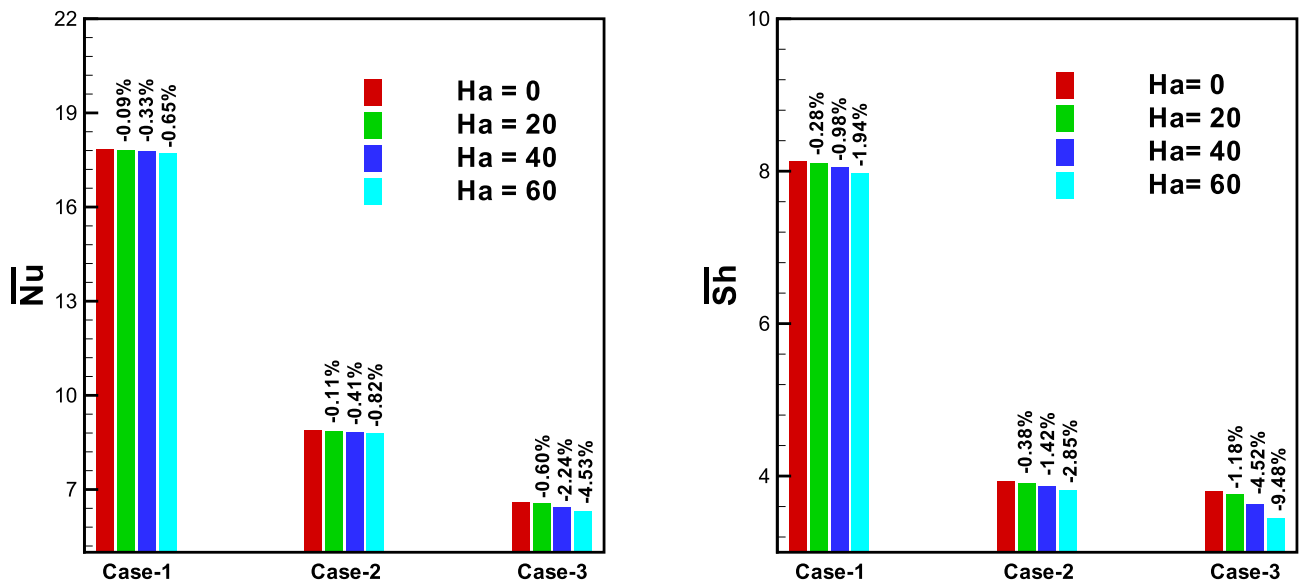


Fig. 21. The bar chart represents variation of average Nusselt number (\overline{Nu}) and average Sherwood number (\overline{Sh}) with Hartmann number (Ha) for different cases and $\phi_{hnp} = 0.04, Ra = 10^5, Da = 10^{-3}, Le = 1, N = 1$ and $Rd = 1$.

As N increases, buoyancy effects become more pronounced, leading to intensified species and energy transport rates. This, in turn, contributes to an escalation in entropy generation. Simultaneously, the decrease in Be reflects the dominance of buoyancy-induced heat transfer effects over fluid friction, particularly noticeable at $N = 10$, where optimal conditions are achieved.

Examining the role of Da in Table 13 and Figure 26 (b), the correlation between Da and entropy production components becomes apparent. The increase in entropy production values as Da grows is associated with the gradual enhancement of fluid flow within the system. Higher Da values indicate a more permeable medium, allowing for increased convective heat and mass transfer. The decline in Be at higher Da values signifies a shift in irreversibility sources, with fluid friction playing a more dominant role.

Moving on to Table 14 and Figure 26 (c), the impact of Ha on entropy productions and the Bejan number is explored. The observed decreasing trend in E_{HT}, E_{MT}, E_{FF} and Be as Ha increases can be attributed to the suppression of electromagnetic forces. A higher Ha implies stronger magnetic fields, limiting the convective

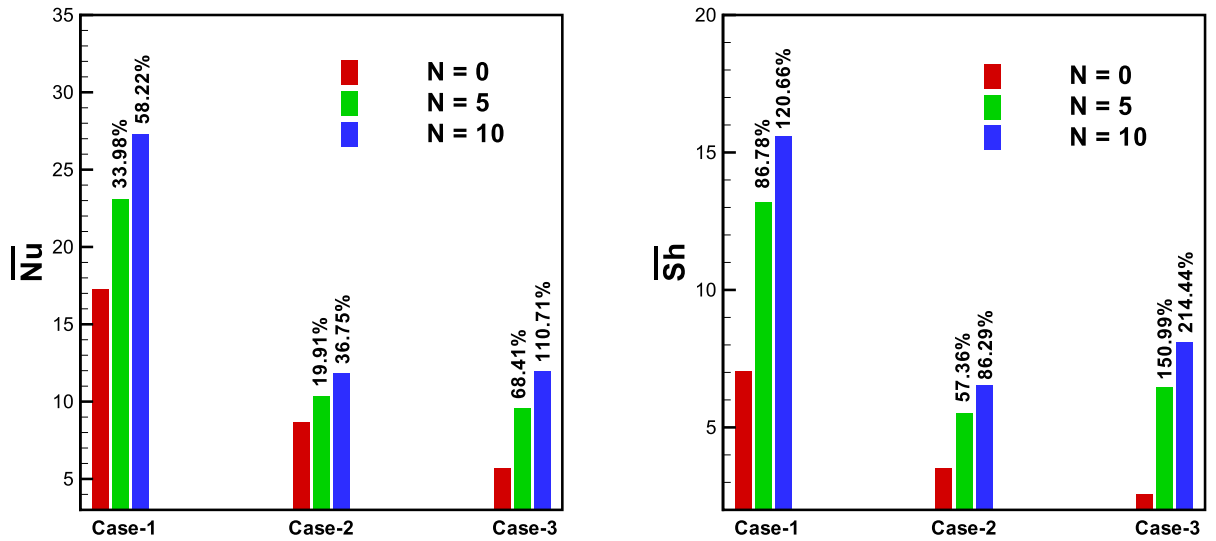


Fig. 22. The bar chart represents variation of average Nusselt number (\overline{Nu}) and average Sherwood number (\overline{Sh}) with buoyancy ratio number (N) for different cases and $\phi_{hnp} = 0.04$, $Ra = 10^5$, $Da = 10^{-3}$, $Le = 1$, $Ha = 25$ and $Rd = 1$.

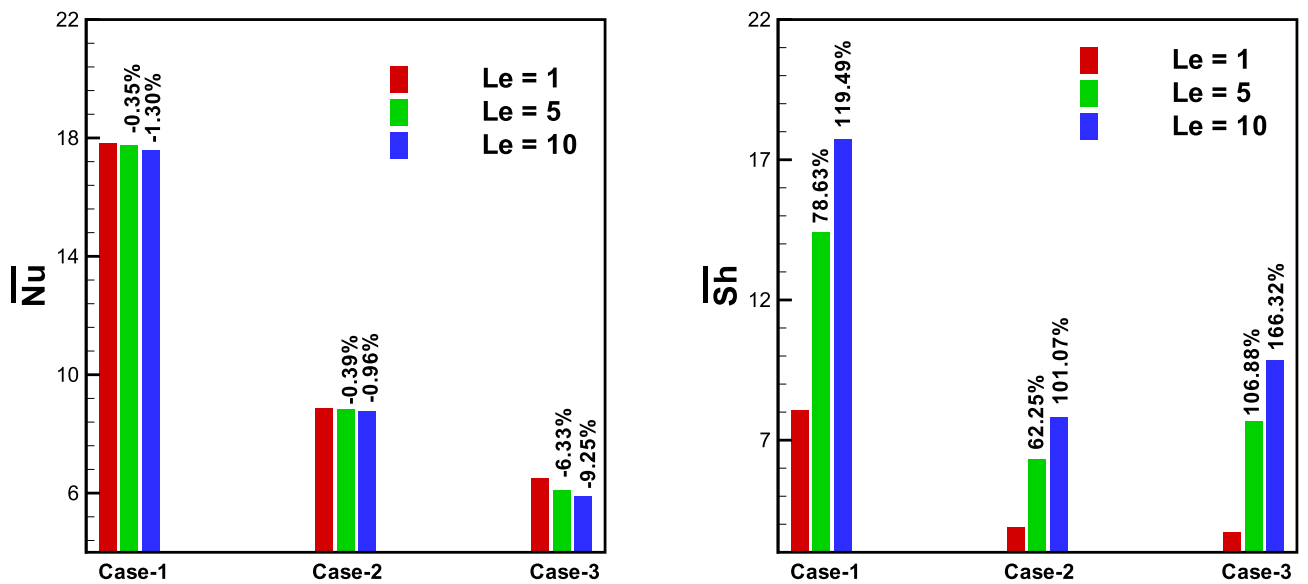


Fig. 23. The bar chart represents variation of average Nusselt number (\overline{Nu}) and average Sherwood number (\overline{Sh}) with Lewis number (Le) for different cases and $Ra = 10^5$, $\phi_{hnp} = 0.04$, $Da = 10^{-3}$, $Ha = 30$, $N = 1$ and $Rd = 1$.

species and energy transport, thus reducing entropy production. Conversely, the increasing trend in E_{MF} and E_T suggests a heightened influence of mechanical friction under stronger magnetic fields. The optimal conditions at $Ha = 60$ indicate a delicate balance where electromagnetic effects are minimized.

Finally, in Table 15, the interplay between Le and entropy production components is discussed. The reduction in E_{HT} , E_{MF} , E_{FF} and E_T with increasing Le signifies a shift towards a more dominant role of species transfer over heat transfer. Higher Le values imply slower diffusion of heat compared to species, leading to decreased entropy production in heat-dominated processes. On the other hand, the improvement in E_{MT} and Be suggests that mass transfer becomes more efficient relative to heat transfer with increasing Le . This delicate balance between energy and species transfer mechanisms unveils the intricate physics governing entropy generation within the studied cases.

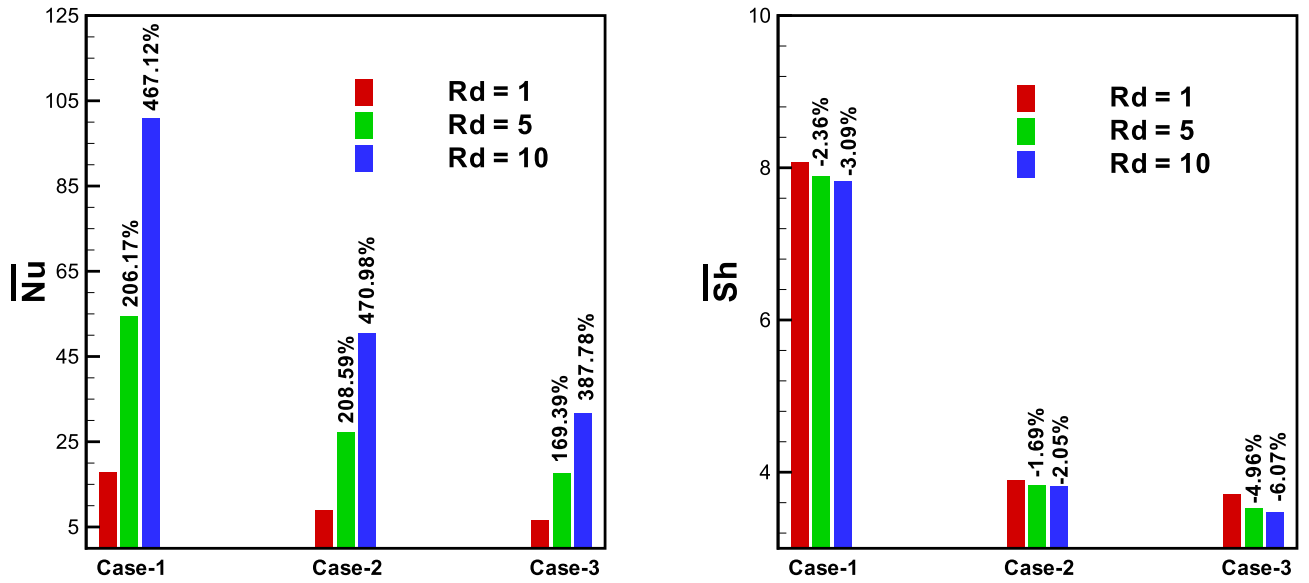


Fig. 24. The bar chart represents variation of average Nusselt number (\overline{Nu}) and average Sherwood number (\overline{Sh}) with radiation parameter (Rd) for different cases and $Ra = 10^5$, $\phi_{hnp} = 0.04$, $Da = 10^{-3}$, $Ha = 25$, $N = 1$ and $Le = 1$.

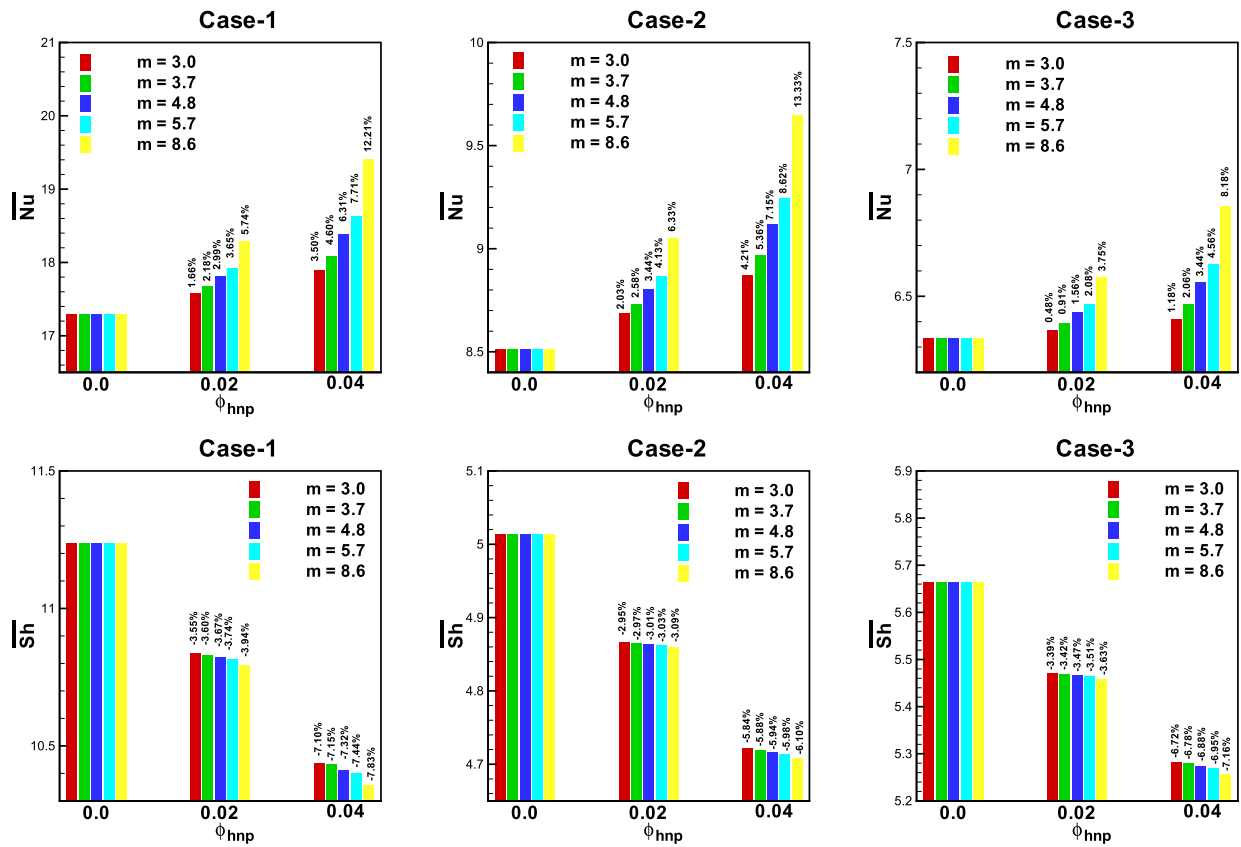


Fig. 25. The bar chart represents variation of average Nusselt number (\overline{Nu}) and average Sherwood number (\overline{Sh}) with the nanoparticle shape factors (m) and solid volume fraction ($\phi_{hnp} = 0.04$) for different cases and $Ra = 10^5$, $\phi_{hnp} = 0.04$, $Da = 10^{-3}$, $Ha = 25$, $N = 1$ and $Le = 1$.

	Ra	E_{HT}	E_{MT}	E_{MF}	E_{FF}	E_T	Be
Case-1	10^4	7.023	3.061	0.015	0.104	10.204	0.988
	10^5	7.260	3.632	2.886	22.006	35.785	0.304
	10^6	11.689	7.352	268.019	1536.609	1826.670	0.010
Case-2	10^4	3.031	1.321	0.006	0.036	4.394	0.990
	10^5	3.070	1.438	1.087	7.436	13.033	0.346
	10^6	4.550	2.717	88.325	747.416	843.009	0.008
Case-3	10^4	1.787	0.780	0.016	0.084	2.668	0.961
	10^5	1.937	1.151	3.355	16.392	22.836	0.135
	10^6	4.736	3.442	209.775	1171.401	1389.356	0.005

Table 11. Variation of E_{HT} , E_{MT} , E_{MF} , E_{FF} , E_T , and Be for different Ra with $\phi_{hnp} = 0.04$, $Ha = 25$, $Le = 1$, $Da = 10^{-3}$, $N = 1$ and $Rd = 1$.

Conclusion

In this work, we have performed a numerical simulation of thermosolutal hydromagnetic convection inside a porous container spotlighting a T-shaped cold. The fluid consists of a hybrid nanofluid with Cu and Al_2O_3 nanoparticles. The chamber is made up of two vertical curved walls as well as two horizontal plane borders. The lower boundary of the container is subjected to heating and solute injection, while the side walls are kept at cold and low concentration. The upper boundary of the enclosure is treated as adiabatic. All four boundaries of the enclosure remain stationary. Additionally, a T-shaped cold fin is located in the middle of the chamber. An external magnetic field is enforced parallel to gravity. We have considered three distinct heating scenarios: uniform heating and soluting of the bottom wall (Case-1), linear heating and soluting (Case-2), and non-uniform heating and soluting (Case-3). We have validated our in-house code for all the computations with the experimental and numerical results available in the literature. We have studied the effects of the Rayleigh numbers, the Hartmann numbers, the Darcy numbers, the Buoyancy numbers, the Lewis number, the volume concentration of the hybrid nanoparticles, and the radiation parameters on fluid flow topologies, energy, and concentration distributions within the curved walled porous chamber. Some of the important findings of the present study are listed below:

- The presence of a T-shaped fin coupled with varied thermal profiles, intricately shapes the flow topology and thermosolutal performance within the porous container.
- Our findings highlight the superior effectiveness of uniform heating (Case-1) compared to linear heating (Case-2) and non-uniform heating (Case-3) in terms of both entropy production and double-diffusion phenomena.
- The optimal thermosolutal performance is achieved with blade-shaped nanoparticles ($m = 8.6$), whereas spherical nanoparticles ($m = 3.0$) exhibit the least favorable performance across all considered aspects.
- The Lewis number (Le) enhances species transfer while diminishing energy transfer within the cabinet. Specifically, an increase in Le from 1 to 10 leads to a significant rise in species transfer by 119.49%, 101.07%, and 166.32% in Case-1, Case-2, and Case-3, respectively. However, this improvement in species transfer comes at the cost of thermal performance, which declines by 1.30%, 0.96%, and 9.25% in the corresponding cases.
- The thermodynamic behavior of the system is strongly governed by the buoyancy ratio number (N), Darcy number (Da), and Rayleigh number (Ra), which control the balance between thermal and solutal convection, permeability effects, and buoyancy-driven instabilities. Increasing N , Da , and Ra enhances convective transport, leading to higher \overline{Nu} , \overline{Sh} , and entropy generation (E_T). The optimal transport performance occurs at $N = 10$, $Da = 10^{-1}$, and $Ra = 10^6$ in all cases, highlighting the dominance of buoyancy-induced flow structures.
- Radiative heat transfer significantly impacts thermal transport by intensifying radiative energy exchange and amplifying temperature gradients. As Rd increases, \overline{Nu} rises, marking a transition toward radiation-dominated heat transfer. Notably, for Rd increasing from 1 to 10, \overline{Nu} surges by 467.12%, 470.98%, and 387.78% in Case-1, Case-2, and Case-3, respectively, underscoring the growing influence of radiative mechanisms.

This study presents a comprehensive investigation of thermosolutal hydromagnetic convection within a porous wavy container featuring a T-shaped cold zone. Future research could extend this work by examining the thermosolutal behavior of non-Newtonian nanofluids in such cavities, particularly under the influence of external factors such as an inclined magnetic field or thermal radiation. This would provide a deeper understanding of their performance under complex conditions. Furthermore, exploring the effects of varying porosity and different nanofluids on heat and mass transfer efficiency could offer valuable insights for optimizing energy systems.

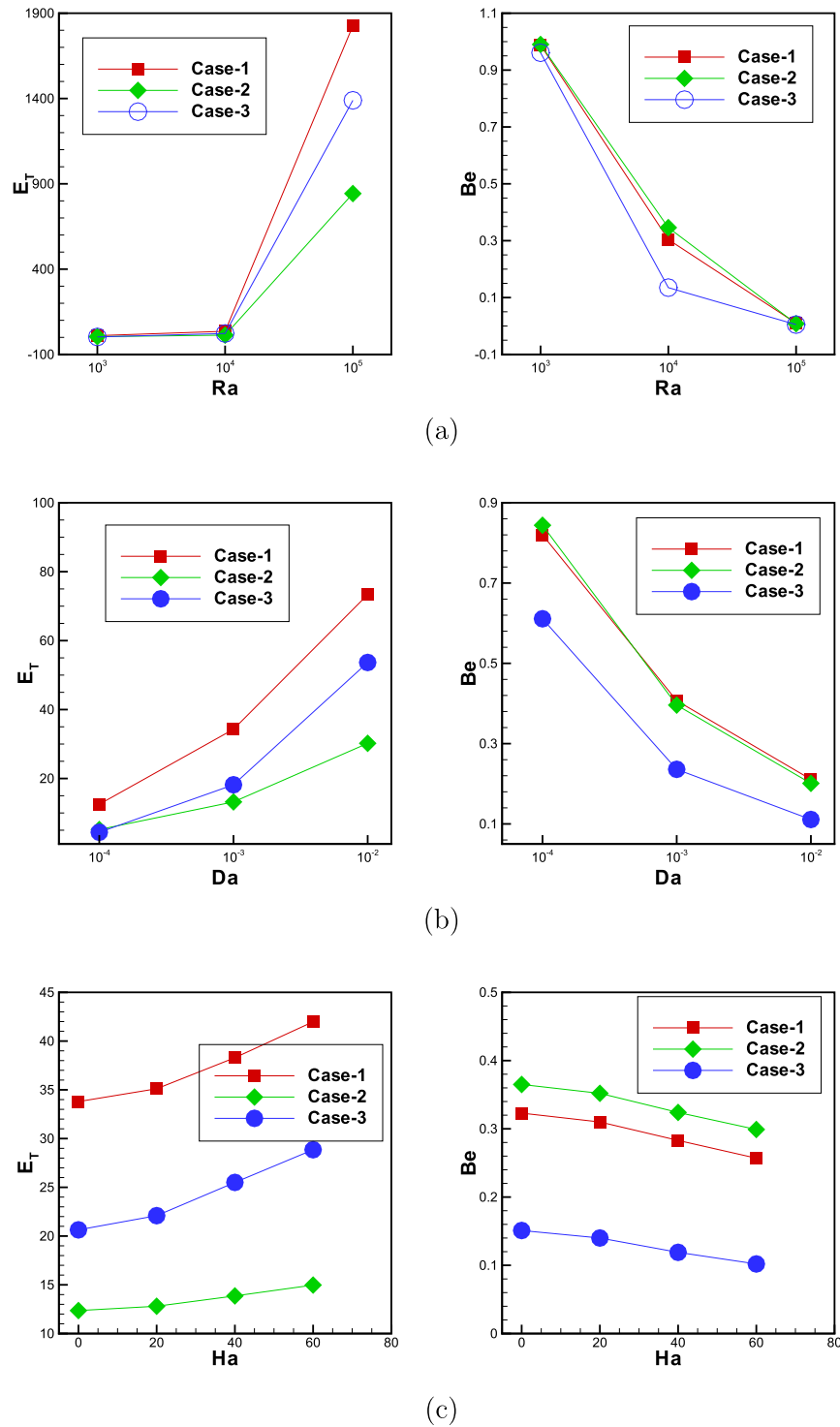


Fig. 26. Variation of total entropy generation (E_T) and Bejan number (Be) for different cases (a) different Rayleigh number (Ra) with $\phi_{hnp} = 0.04$, $Ha = 25$, $Le = 1$, $Da = 10^{-3}$, $N = 1$ and $Rd = 1$ (b) different Darcy number (Da) with $\phi_{hnp} = 0.04$, $Ra = 10^5$, $Ha = 25$, $Le = 5$, $N = 1$ and $Rd = 1$ and (c) different Hartmann number (Ha) with $\phi_{hnp} = 0.04$, $Ra = 10^5$, $Da = 10^{-3}$, $Le = 1$, $N = 1$ and $Rd = 1$.

	N	E_{HT}	E_{MT}	E_{MF}	E_{FF}	E_T	Be
Case-1	0	7.043	3.160	0.473	3.204	13.881	0.735
	5	9.481	6.140	22.001	272.349	309.974	0.050
	10	11.304	7.374	51.800	678.647	749.125	0.024
Case-2	0	3.032	1.334	0.171	1.041	5.580	0.782
	5	3.459	1.947	11.412	94.526	111.346	0.048
	10	3.852	2.271	30.080	253.611	289.815	0.021
Case-3	0	1.800	0.840	0.504	2.503	5.647	0.467
	5	2.697	2.077	29.551	155.941	190.268	0.025
	10	3.391	2.669	73.329	49.465	488.855	0.012

Table 12. Variation of E_{HT} , E_{MT} , E_{MF} , E_{FF} , E_T , and Be for different N with $\phi_{hnp} = 0.04$, $Ra = 10^5$, $Da = 10^{-3}$, $Le = 1$, $Ha = 25$ and $Rd = 1$.

	Da	E_{HT}	E_{MT}	E_{MF}	E_{FF}	E_T	Be
Case-1	10^{-4}	7.019	3.259	0.041	2.205	12.526	0.820
	10^{-3}	7.243	6.727	1.670	18.643	34.284	0.407
	10^{-2}	8.019	7.483	22.657	35.190	73.350	0.211
Case-2	10^{-4}	3.029	1.359	0.016	0.790	5.195	0.844
	10^{-3}	3.065	2.167	0.956	7.016	13.205	0.396
	10^{-2}	3.320	2.765	8.199	15.915	30.201	0.201
Case-3	10^{-4}	1.786	0.903	0.043	1.668	4.401	0.611
	10^{-3}	1.863	2.438	2.243	11.632	18.179	0.236
	10^{-2}	2.512	3.490	21.128	26.534	53.665	0.111

Table 13. Variation of E_{HT} , E_{MT} , E_{MF} , E_{FF} , E_T , and Be for different Da with $\phi_{hnp} = 0.04$, $Ra = 10^5$, $Ha = 25$, $Le = 5$, $N = 1$ and $Rd = 1$.

	Ha	E_{HT}	E_{MT}	E_{MF}	E_{FF}	E_T	Be
Case-1	0	7.270	3.648	0.000	22.876	33.794	0.323
	20	7.247	3.647	1.902	22.304	35.109	0.310
	40	7.247	3.611	6.590	20.847	38.297	0.283
	60	7.226	3.575	12.297	18.880	41.979	0.257
Case-2	0	3.073	1.444	0.000	7.840	12.358	0.365
	20	3.071	1.440	0.715	7.576	12.804	0.352
	40	3.067	1.431	2.480	6.884	13.862	0.324
	60	3.061	1.417	4.524	5.972	14.975	0.299
Case-3	0	1.950	1.174	0.000	17.515	20.638	0.151
	20	1.942	1.160	2.209	16.783	22.094	0.140
	40	1.919	1.118	7.620	14.844	25.5025	0.119
	60	1.888	1.059	13.617	12.287	28.853	0.102

Table 14. Variation of E_{HT} , E_{MT} , E_{MF} , E_{FF} , E_T , and Be for different Ha with $\phi_{hnp} = 0.04$, $Ra = 10^5$, $Da = 10^{-3}$, $Le = 1$, $N = 1$ and $Rd = 1$.

	Le	E_{HT}	E_{MT}	E_{MF}	E_{FF}	E_T	Be
Case-1	1	7.256	3.625	4.016	21.659	36.558	0.297
	5	7.241	6.717	2.372	18.476	34.807	0.401
	10	7.174	8.325	1.699	13.739	30.940	0.500
Case-2	1	3.069	1.436	1.513	7.271	13.291	0.339
	5	3.064	2.162	1.342	6.917	13.486	0.387
	10	3.054	2.627	1.032	5.317	12.031	0.472
Case-3	1	1.932	1.142	4.668	15.932	23.675	0.129
	5	1.861	2.429	3.154	11.427	18.872	0.227
	10	1.831	3.517	2.257	8.469	15.715	0.317

Table 15. Variation of E_{HT} , E_{MT} , E_{MF} , E_{FF} , E_T , and Be for different Le with $Ra = 10^5$, $\phi_{hnp} = 0.04$, $Da = 10^{-3}$, $Ha = 30$, $N = 1$ and $Rd = 1$.

Data availability

The datasets used and/or analysed during the current study are available from the corresponding author on reasonable request.

Received: 26 December 2024; Accepted: 15 May 2025

Published online: 29 September 2025

References

- Hansda, S. & Pandit, S. K. On the analysis of thermosolutal mixed convection with thermophoresis effects in a wavy porous cabine. *Numerical Heat Transfer, Part A: Applications*. **85**(16), 2640–2663 (2023).
- Hansda, S., Chattopadhyay, A. & Pandit, S. K. Analysis of thermosolutal performance and entropy generation for ternary hybrid nanofluid in a partially heated wavy porous cabinet. *International Journal of Numerical Methods for Heat & Fluid Flow* **34**(2), 709–740 (2023).
- Bilal, S., Shah, I.A., Khan, I., Otaibi, S. Al. & Rahimzai, A. A. FEM simulations for double diffusive transport mechanism hybrid nano fluid flow in corrugated enclosure by installing uniformly heated and concentrated cylinder. *Scientific Reports*. **14**(1), 766 (2024).
- Mohamed, R. A., Abo-Dahab, S. M., Abd-Alla, A. M. & Soliman, M. S. Magneto-hydrodynamic double-diffusive peristaltic flow of radiating fourth-grade nanofluid through a porous medium with viscous dissipation and heat generation/absorption. *Scientific Reports*. **13**(1), 13096 (2023).
- Bahram, J., Emad, M., Malekshah, E., H., Jalili, P., Akg?l, A. & Hassani, M., M. Investigating double-diffusive natural convection in a sloped dual-layered homogenous porous-fluid square cavity. *Scientific Reports*. **14**(1), 7193 (2024).
- Baithalu, R., Panda, S., Pattnaik, P. K. & Mishra, S. R. Blood-Based CNT Nanofluid Flow Over Rotating Discs for the Impact of Drag Using Darcy?Forchheimer Model Embedding in Porous Matrix. *International Journal of Applied and Computational Mathematics* **10**(3), 1–20 (2024).
- Panda, S., Baithalu, R., Pattnaik, P.K., & Mishra, S.R. Illustration of slip velocity on the radiative hybrid nanofluid flow over an elongating/contracting surface with dissipative heat effects. *Journal of Thermal Analysis and Calorimetry* 1-12 (2024).
- Baithalu, R., Mishra, S. R. & Panda, S. Magnetic dissipation on radiative free convection of a conducting hybrid nanofluid within a rotating cone and circular disc. *Partial Differential Equations in Applied Mathematics* **11**, 100788 (2024).
- Panda, S., Pattnaik, P.K., Baithalu, R., & Mishra, S.R. Inertial drag combined with non-uniform heat generation/absorption effects on the hydromagnetic flow of polar nanofluid over an elongating permeable surface due to the impose of chemical reaction. *ZAMM-Journal of Applied Mathematics and Mechanics/Zeitschrift f?r Angewandte Mathematik und Mechanik* **104**(9), e202301058 (2024).
- Mishra, S. R., Pattnaik, P. K., Baithalu, R., Ratha, P. K. & Panda, S. Predicting heat transfer Performance in transient flow of CNT nanomaterials with thermal radiation past a heated spinning sphere using an artificial neural network: A machine learning approach. *Partial Differential Equations in Applied Mathematics* **12**, 100936 (2024).
- Pattnaik, P.K., Mishra, S.R., Baithalu, R., & Panda, S. Sensitivity analysis and enhanced EMHD performance of unsteady ferrite-water hybrid nanofluid on a Riga plate with variable magnetization and heat generation. *Numerical Heat Transfer, Part A: Applications* 1-23 (2024).
- Khan, W.A. Significance of magnetized Williamson nanofluid flow for ferromagnetic nanoparticles. *Waves in Random and Complex Media* 1-20 (2023).
- Khan, W.A. Impact of time-dependent heat and mass transfer phenomenon for magnetized Sutterby nanofluid flow. *Waves in random and complex media* 1-15 (2022).
- Khan, W.A. Dynamics of gyrotactic microorganisms for modified Eyring Powell nanofluid flow with bioconvection and nonlinear radiation aspects. *Waves in Random and Complex Media* 1-11 (2023).
- Irfan, M. et al. Significance of non-Fourier heat flux on ferromagnetic Powell-Eyring fluid subject to cubic autocatalysis kind of chemical reaction. *International Communications in Heat and Mass Transfer* **138**, 106374 (2022).
- Nazash, A. et al. Numerical analysis for thermal performance of modified Eyring Powell nanofluid flow subject to activation energy and bioconvection dynamic. *Case Studies in Thermal Engineering* **39**, 102427 (2022).
- Tabrez, M., & Khan, W.A. Exploring physical aspects of viscous dissipation and magnetic dipole for ferromagnetic polymer nanofluid flow. *Waves in random and complex media* 1-20 (2022).
- Waqas, M., Khan, W. A., Pasha, A. A., Islam, N. & Rahman, M. M. Dynamics of bioconvective Casson nanofluid from a moving surface capturing gyrotactic microorganisms, magnetohydrodynamics and stratifications. *Thermal Science and Engineering Progress* **36**, 101492 (2022).
- Hussain, Z., & Khan, W.A. Impact of thermal-solutal stratifications and activation energy aspects on time-dependent polymer nanofluid. *Waves in random and complex media* 1-11 (2022).
- Khan, W. A. et al. Impact of nanoparticles and radiation phenomenon on viscoelastic fluid. *International Journal of Modern Physics B* **36**(05), 2250049 (2022).

21. Khan, W. A. et al. On the evaluation of stratification based entropy optimized hydromagnetic flow featuring dissipation aspect and Robin conditions. *Computer Methods and Programs in Biomedicine* **190**, 105347 (2020).
22. Kumar, S., Gangawane, K. M. & Oztop, H. F. Applications of lattice Boltzmann method for double-diffusive convection in the cavity: A review. *Journal of Thermal Analysis and Calorimetry*. **147**(20), 10889–10921 (2022).
23. Corcione, M., Grignaffini, S. & Quintino, A. Correlations for the double-diffusive natural convection in square enclosures induced by opposite temperature and concentration gradients. *International Journal of Heat and Mass Transfer* **81**, 811–819 (2015).
24. Rashid, U., Shahzad, H., Lu, D., Wang, X. & Majeed, A. H. Non-Newtonian MHD double diffusive natural convection flow and heat transfer in a crown enclosure. *Case Studies in Thermal Engineering*. **41**, 102541 (2023).
25. Aly, A. M., Mohamed, E. M. & Alsedais, N. Double-diffusive convection from a rotating rectangle in a finned cavity filled by a nanofluid and affected by a magnetic field. *International Communications in Heat and Mass Transfer* **126**, 105363 (2021).
26. Moderres, M., Abboudi, S., Ihdene, M., Aberkane, S. & Ghezal, A. Numerical investigation of double-diffusive mixed convection in horizontal annulus partially filled with a porous medium. *International Journal of Numerical Methods for Heat & Fluid Flow* **27**(4), 773–794 (2017).
27. Aly, A. M., Alsedais, N. & Oztop, H. F. Effects of a magnetic field on double-diffusive convection of a nanofluid in a cavity saturated by wavy layers of porous media: ISPH analysis. *International Journal of Numerical Methods for Heat & Fluid Flow* **32**(3), 1046–1066 (2022).
28. Aly, A. M. & Mohamed, E. M. Effects of buoyancy ratio on diffusion of solid particles inside a pipe during double diffusive flow of a nanofluid. *International Journal of Numerical Methods for Heat & Fluid Flow* **31**(6), 1951–1986 (2021).
29. Elshehaby, H. M., Colak, A. B. & Aly, A. M. Adjoined ISPH method and artificial intelligence for thermal radiation on double diffusion inside a porous L-shaped cavity with fins. *International Journal of Numerical Methods for Heat & Fluid Flow* **34**(4), 1832–1857 (2024).
30. Chamkha, A. J. & Al-Naser, H. Hydromagnetic double-diffuse convection in a rectangular enclosure with opposing temperature and concentration gradients. *Int. J. Heat Mass Transfer*. **45**, 2465–2483 (2002).
31. Teamah & M. A. Numerical simulation of double diffusive natural convection in rectangular enclosure in the presences of magnetic field and heat source. *Int. J. Therm. Sci.* **47**(3), 237–248 (2008).
32. Hansda, S. & Pandit, S. K. Thermosolutal hydromagnetic mixed convective hybrid nanofluid flow in a wavy walled enclosure. *Journal of Magnetism and Magnetic Materials*. **572**, 170580 (2023).
33. Srinivasacharya, D. & Ramana, K. S. Thermal radiation and double diffusive effects on bioconvection flow of a nanofluid past an inclined wavy surface. *Thermal Science and Engineering Progress*. **22**, 100830 (2021).
34. Ibrahim, A. & Lemonnier, D. Numerical study of coupled double-diffusive natural convection and radiation in a square cavity filled with a N₂?CO₂ mixture. *International Communications in Heat and Mass Transfer*. **36**(3), 197–202 (2009).
35. Moufekkir, F., Moussaoui, M. A., Mezrhab, A., Bouzidi, M. & Laraqi, N. Study of double-diffusive natural convection and radiation in an inclined cavity using lattice Boltzmann method. *International Journal of Thermal Sciences*. **63**, 65–86 (2013).
36. Abidi, A., Kolsi, L., Borjini, M. N. & Aissia, H. B. Effect of radiative heat transfer on three-dimensional double diffusive natural convection. *Numerical Heat Transfer, Part A: Applications*. **60**(9), 785–809 (2011).
37. Mohammadi, M. & Nassab, S. A. G. Double-diffusive convection flow with Soret and Dufour effects in an irregular geometry in the presence of thermal radiation. *International Communications in Heat and Mass Transfer*. **134**, 106026 (2022).
38. Rashad, A. M., Ahmed, S. E. & Mansour, A. M. Effects of chemical reaction and thermal radiation on unsteady double diffusive convection. *International Journal of Numerical Methods for Heat & Fluid Flow* **24**(5), 1124–1140 (2014).
39. Abderrahmane, A. et al. The baffle shape effects on natural convection flow and entropy generation in a nanofluid-filled permeable container with a magnetic field. *Scientific Reports*. **14**(1), 2550 (2024).
40. Rehman, N., Mahmood, R., Majeed, A. H., Khan, I. & Mohamed, A. Multigrid simulations of non-Newtonian fluid flow and heat transfer in a ventilated square cavity with mixed convection and baffles. *Scientific Reports*. **14**(1), 6694 (2024).
41. Chamkha, A. J., Mansour, M. A. & Ahmed, S. E. Double-diffusive natural convection in inclined finned triangular porous enclosures in the presence of heat generation/absorption effects. *Heat and mass transfer* **46**, 757–768 (2010).
42. Al-Farhany, K. et al. Magnetohydrodynamic double-diffusive mixed convection in a curvilinear cavity filled with nanofluid and containing conducting fins. *International Communications in Heat and Mass Transfer* **144**, 106802 (2023).
43. Eshaghi, S. et al. The optimum double diffusive natural convection heat transfer in H-Shaped cavity with a baffle inside and a corrugated wall. *Case Studies in Thermal Engineering* **28**, 101541 (2021).
44. Nayak, M. K. et al. Efficacy of diverse structures of wavy baffles on heat transfer amplification of double-diffusive natural convection inside a C-shaped enclosure filled with hybrid nanofluid. *Sustainable Energy Technologies and Assessments* **52**, 102180 (2022).
45. Alsedais, N. & Aly, A. M. Double-diffusive convection from an oscillating baffle embedded in an astroid-shaped cavity suspended by nano encapsulated phase change materials: ISPH simulations, *Waves in Random and Complex Media* 1–20 (2021).
46. Irshad, K. et al. Hydrothermal behavior and entropy analysis of double-diffusive nano-encapsulated phase change materials in a porous wavy H-shaped cavity with baffles: Effect of thermal parameters. *Journal of Energy Storage* **72**, 108250 (2023).
47. Ishak, M. S., Alsabery, A. I., Hashim, I. & Chamkha, A. J. Entropy production and mixed convection within trapezoidal cavity having nanofluids and localised solid cylinder. *Scientific reports* **11**(1), 14700 (2021).
48. Bejan, A. *Entropy Generation Minimization*, CRC Press (Fl, 1982).
49. Zahor, F. A., Jain, R., Ali, A. O. & Masanja, V. G. ?Modeling entropy generation of magnetohydrodynamics flow of nanofluid in a porous medium: a review. *International Journal of Numerical Methods for Heat and Fluid Flow* **33**(2), 751–771 (2023).
50. Sheremet, M. A., Pop, I., Oztop, H. F. & Abu-Hamdeh, N. Natural convection of nanofluid inside a wavy cavity with a non-uniform heating: entropy generation analysis. *International Journal of Numerical Methods for Heat & Fluid Flow* **27**(4), 958–980 (2017).
51. KhakRah, H. R., Hooshmand, P., Ross, D. & Jamshidian, M. “Numerical analysis of free convection and entropy generation in a cavity using compact finite-difference lattice Boltzmann method. *International Journal of Numerical Methods for Heat & Fluid Flow* **30**(2), 977–995 (2020).
52. Shirvan, K. M., Mirzakhani, S., Oztop, H. F., Mamourian, M. & Al-Salem, K. MHD heat transfer and entropy generation in inclined trapezoidal cavity filled with nanofluid: numerical investigation and sensitivity analysis. *International Journal of Numerical Methods for Heat & Fluid Flow* **27**(10), 2174–2202 (2017).
53. Tayebi, T. & Chamkha, A. J. Entropy generation analysis during MHD natural convection flow of hybrid nanofluid in a square cavity containing a corrugated conducting block. *International Journal of Numerical Methods for Heat & Fluid Flow* **30**(3), 1115–1136 (2020).
54. Ishak, M. S., Alsabery, Chamkha, A. J., & Hashim, I. Effect of finite wall thickness on entropy generation and natural convection in a nanofluid-filled partially heated square cavity, *International Journal of Numerical Methods for Heat & Fluid Flow* **30**(3), 1518–1546 (2020).
55. Magherbi, M., Abbassi, H., Hidouri, N. & Brahim, A. B. Second law analysis in convective heat and mass transfer. *Entropy* **8**, 1–17 (2006).
56. Mchirgui, A., Hidouri, N., Magherbi, M. & Brahim, A. B. “Entropy Generation in Double-Diffusive Convection in a Square Porous Cavity using Darcy-Brinkman Formulation. *Transp Porous Med.* **93**, 223–240 (2021).
57. Oueslati, F., Ben-Beya, B. & Lili, T. Double-diffusive natural convection and entropy generation in an enclosure of aspect ratio 4 with partial vertical heating and salting sources. *Alexandria Engineering Journal* **52**(4), 605–625 (2013).
58. Ghachem, K., Kolsi, L., Maatki, C., Hussein, A. K. & Borjini, M. N. Numerical simulation of three-dimensional double diffusive free convection flow and irreversibility studies in a solar distiller. *Int. Commun. Heat Mass Transfer* **39**, 869–876 (2012).

59. Ababaei, A., Abbaszadeh, M., Arefmanesh, A. & Chamkha, A. J. Numerical simulation of double-diffusive mixed convection and entropy generation in a lid-driven trapezoidal enclosure with a heat source. *Numerical Heat Transfer, Part A: Applications* **73**(10), 702–720 (2018).
60. Hussain, S., Mehmood, K., Sagheer, M. & Yamin, M. Numerical simulation of double diffusive mixed convective nanofluid flow and entropy generation in a square porous enclosure. *International Journal of Heat and Mass Transfer* **122**, 1283–1297 (2018).
61. Hansda, S. & Pandit, S. K. On the analysis of thermosolutal mixed convection in differentially heated and soluted geometries beyond rectangular. *International Journal of Numerical Methods for Heat & Fluid Flow* **33**(8), 2877–2901 (2023).
62. Pandit, S. K. & Chattopadhyay, A. “A robust higher order compact scheme for solving general second order partial differential equation with derivative source terms on nonuniform curvilinear meshes. *Computers & Mathematics with Applications* **74**(6), 1414–1434 (2017).
63. Pandit, S. K., Kalita, J. C. & Dalal, D. C. A fourth-order accurate compact scheme for the solution of steady Navier-Stokes equations on non-uniform grids. *Computer & Fluids* **37**(2), 121–134 (2008).
64. Pandit, S. K., Chattopadhyay, A. & Oztop, H. F. A fourth order compact scheme for heat transfer problem in porous media. *Computers & Mathematics with Applications* **71**(3), 805–832 (2016).
65. Lele, S. K. Compact finite difference schemes with spectral like resolution. *J. Comput. Phys.* **103**, 16–42 (1992).
66. Van Der Vorst, H. (1992), BiCGSTAB: A fast and smoothly converging variant of BiCG for the solution of nonsymmetric linear systems. *SIAM J. Sci. Comput.* **13**, 631–644 (1992).
67. Al-Amiri, A. M., Khanafer, K. & Pop, I. Numerical simulation of combined thermal and mass transport in a square lid-driven cavity. *International Journal of Thermal Sciences* **46**, 662–671 (2007).
68. Mahmud, S., Das, P. K., Hyder, N. & Islam, A. K. M. S. Free convection in an enclosure with vertical wavy walls. *International Journal of Thermal Sciences* **41**, 440–446 (2002).
69. Sompong, P. & Witayangkurn, S. Simulation of natural convection in a complicated enclosure with two wavy vertical walls. *Applied Mathematical Sciences* **6**(57), 2833–2842 (2012).
70. Ma, Y., Mohebbi, R., Rashidi, M. M., Yang, Z. & Sheremet, M. A. Numerical study of MHD nanofluid natural convection in a baffled U-shaped enclosure. *Int. J. Heat mass transf.* **130**, 123–134 (2019).
71. Corvaro, F. & Paroncini, M. Experimental analysis of natural convection in square cavities heated from below with 2D-PIV and holographic interferometry techniques. *Exp. Therm. Fluid Sci.* **31**, 721–739 (2007).
72. Iliis, G. G., Mobedi, M. & Sunden, B. Effect of aspect ratio on entropy generation in a rectangular cavity with differentially heated vertical walls. *Int. Commun. Heat Mass Transfer* **35**, 696–703 (2008).
73. Bettaibi, S., Kuznik, F. & Sediki, E. Hybrid LBM-MRT model coupled with finite difference method for double-diffusive mixed convection in rectangular enclosure with insulated moving lid”. *Physica A: Statistical Mechanics and its Applications* **444**, 311–326 (2016).
74. Abu-Nada, E. & Chamkha, A. J. Mixed convection flow in a lid-driven inclined square enclosure filled with a nanofluid. *European Journal of Mechanics B/Fluids* **29**, 472–482 (2010).
75. Ho, C. J., Liu, W. K., Chang, Y. S. & Lin, C. C. Natural convection heat transfer of aluminawater nanofluid in vertical square enclosures: an experimental study. *Int. J. Therm. Sci.* **49**, 1345–1353 (2010).
76. Saghir, M. Z., Ahadi, A., Mohamad, A. & Srinivasan, S. Water aluminum oxide nanofluid benchmark model. *Int. J. Therm. Sci.* **109**, 148–158 (2016).
77. Ghasemi, B., Aminossadati, S. M. & Raisi, A. Magnetic field effect on natural convection in a nanofluid-filled square enclosure. *Int J Therm Sci.* **50**(9), 1748–1756 (2011).
78. Revnic, C., Grosan, T., Sheremet, M. A. & Pop, I. Numerical simulation of MHD natural convection flow in a wavy cavity filled by a hybrid Cu-Al₂O₃ water nanofluid with discrete heating. *Appl Math Mech.* **41**, 1345–1358 (2020).
79. Hansda, S., Pandit, S. K. & Sheu, T. W. H. Thermosolutal discharge of double diffusion mixed convection flow with Brownian motion of nanoparticles in a wavy chamber. *J. Therm. Anal. Calorim.* **147**, 7007–7029 (2022).
80. Hansda, S. & Pandit, S. K. Performance of thermosolutal discharge for double diffusive mixed convection of hybrid nanofluid in a lid driven concave-convex chamber. *Journal of Thermal Analysis and Calorimetry* **148**(3), 1109–1131 (2023).
81. Hansda, S., Chattopadhyay, A. & Pandit, S. K. Optimizing thermosolutal and hydrothermal performance of radiative hybrid ferrofluid and entropy generation in a wavy porous enclosure. *Journal of Magnetism and Magnetic Materials* **592**, 171774 (2024).
82. Hansda, S. Effect of thermal radiation and inclined magnetic field on thermosolutal mixed convection in a partially active wavy trapezoidal enclosure filled with hybrid nanofluid. *International Journal of Thermofluids* **24**, 100888 (2024).
83. Hansda, S., Chattopadhyay, A. & Pandit, S. K. Thermosolutal and hydromagnetic performance of radiative hybrid nanofluid in a wavy porous enclosure with a plus-shaped baffle. *Journal of Molecular Liquids* **404**, 124880 (2024).

Acknowledgements

This work of Samrat Hansda was supported by the DST-FIST, Govt of India (File No.: SR/FST/MS-I/2022/123).

Author contributions

Samrat Hansda: Investigation, Validation, Writing—original draft Anirban Chattopadhyay: Supervision, Validation, Writing—original draft Swapan K. Pandit: Conceptualization, Methodology, Supervision, Writing—original draft Hakan F. Oztop: Conceptualization, Writing—original draft.

Declarations

Competing interests

The authors declare that they have no known competing financial interests or personal relationships that could have appeared to influence the work reported in this paper.

Additional information

Correspondence and requests for materials should be addressed to S.H.

Reprints and permissions information is available at www.nature.com/reprints.

Publisher’s note Springer Nature remains neutral with regard to jurisdictional claims in published maps and institutional affiliations.

Open Access This article is licensed under a Creative Commons Attribution-NonCommercial-NoDerivatives 4.0 International License, which permits any non-commercial use, sharing, distribution and reproduction in any medium or format, as long as you give appropriate credit to the original author(s) and the source, provide a link to the Creative Commons licence, and indicate if you modified the licensed material. You do not have permission under this licence to share adapted material derived from this article or parts of it. The images or other third party material in this article are included in the article's Creative Commons licence, unless indicated otherwise in a credit line to the material. If material is not included in the article's Creative Commons licence and your intended use is not permitted by statutory regulation or exceeds the permitted use, you will need to obtain permission directly from the copyright holder. To view a copy of this licence, visit <http://creativecommons.org/licenses/by-nc-nd/4.0/>.

© The Author(s) 2025